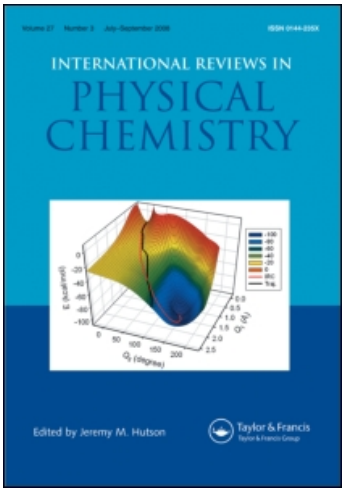

International Reviews in Physical Chemistry
Publication details, including instructions for authors and subscription information:
http://www.informaworld.com/smpp/title~content=t713724383

Hyperthermal chemistry in the gas phase and on surfaces: theoretical studies

Diego Troya[a]; George C. Schatz[a]
[a] Department of Chemistry, Northwestern University, Evanston, IL 60208-3113, USA

To cite this Article Troya, Diego and Schatz, George C.(2004) 'Hyperthermal chemistry in the gas phase and on surfaces: theoretical studies', International Reviews in Physical Chemistry, 23: 3, 341 — 373
To link to this Article: DOI: 10.1080/0144235042000298484
URL: http://dx.doi.org/10.1080/0144235042000298484

INT. REVIEWS IN PHYSICAL CHEMISTRY, 2004
VOL. 23, NO. 3, 341–373

Taylor & Francis
Taylor & Francis Group

Hyperthermal chemistry in the gas phase and on surfaces: theoretical studies

DIEGO TROYA* and GEORGE C. SCHATZ†
Department of Chemistry, Northwestern University, Evanston, IL 60208-3113, USA

We review recent theoretical studies aimed at understanding gas/surface and gas-phase collisions at hyperthermal energies. The review is restricted to interactions between neutral species, and particular attention is given to the interactions of hyperthermal ground-state atomic oxygen ($O(^3P)$) with hydrocarbons. Quantum mechanical and molecular dynamics calculations are used to simulate collisions of $O(^3P)$ with gas-phase methane, ethane, and propane molecules and with condensed-phase alkanethiolate self-assembled monolayers. The results of such studies are examined in the light of atomic-oxygen degradation of polymeric materials in low Earth orbit (LEO).

Contents

*Current address: Department of Chemistry, Virginia Tech, 107 Davidson Hall, Blacksburg, VA 24061-0212, USA.
† E-mail: schatz@chem.northwestern.edu

International Reviews in Physical Chemistry ISSN 0144–235X print/ISSN 1366–591X online © 2004 Taylor & Francis Ltd
http://www.tandf.co.uk/journals
DOI: 10.1080/0144235042000298484

1. Introduction

Research on hyperthermal chemistry is an expanding field that is increasing our knowledge about chemical reactivity in systems under conditions that have not been amenable to quantitative study before. Advances both in experimental techniques and in computational capabilities are allowing controlled simulations of hyperthermal processes that are contributing to our understanding of how chemical reactions occur in extreme conditions. Here we review recent advances in the use and understanding of hyperthermal collisions between gas-phase species or between a hyperthermal gas-phase atom or molecule and a condensed-phase surface, with particular emphasis on theoretical modelling. We shall especially be concerned with novel, high-barrier reaction mechanisms that are not accessible under normal laboratory conditions but which play a significant role in the overall dynamics behaviour of the system at hyperthermal energies.

The hyperthermal energy regime has not been uniquely defined. In this paper we will be mainly concerned with processes occurring at collision energies in the 1–10 eV range, and this will be our definition of the hyperthermal energy regime. In general, the hyperthermal energy regime allows for chemical processes that are not possible under normal laboratory conditions or even in combustion experiments. However, hyperthermal processes should be distinguished from other processes that take place at much higher energies (in the keV range) and which mainly have a physical nature, such as sputtering.

In the past, the problem of generating species at velocities greatly exceeding room-temperature motion in the laboratory has been solved by taking advantage of well-established technology for ion acceleration in an electric field. The widespread use of such techniques has given rise to a large body of experimental literature that has been accompanied by corresponding theoretical simulations. Since there are extensive recent reviews [1, 2] dealing with hyperthermal processes involving ions, we restrict our discussion to hyperthermal collisions involving neutral species.

There is a wide variety of reasons for interest in hyperthermal collisions between neutral gas-phase species or between a neutral gas-phase projectile and a surface. Cluster growth, chemical etching, adhesion improvement, biocompatibility enhancement, oxidation, surface characterization and chemiluminescence are all examples of areas in which neutral hyperthermal chemistry has applied interest. Additionally, the unique dynamics characteristics of processes taking place at hyperthermal energies complement our understanding of reaction dynamics fundamentals.

There are a number of chemical processes that can take place when a gas-phase projectile strikes a condensed-phase surface at hyperthermal energy. Among non-reactive events one can find inelastic processes and collision-induced ionization. Physisorption, chemisorption, surface-induced dissociation and collision-induced desorption are all examples of processes in which chemical reactions (or bond breakage/formation) occur. In the gas phase, inelastic processes characterize non-reactive encounters while bond breakage/formation leads to reaction and collision-induced dissociation.

1.1. *Collision-induced ionization*

Let us begin by summarizing research carried out on hyperthermal processes that do not produce bond formation or breakage. Hyperthermal *collision-induced ionization* is a process whereby the positive or negative ion of an atom or a molecule is produced from collision of the neutral species with a surface. This has been found

abundantly in the laboratory for sodium atoms impinging on metals [3–5], molecular species ranging from I_2 to anthracene colliding with diamond [6, 7], or in the alkali atom/Si(111) system [8]. Ionization of the gas-phase projectile is possible if the initial kinetic energy is effectively used to overcome the ionization potential or the electron affinity of the gas-phase species. In some cases, if the initial collision energy is large enough, metals with ionization potentials as large as that of mercury (10.44 eV) can be ionized [9]. Hyperthermal surface-induced ionization can be associated with substantial energy transfer to internal degrees of freedom of the molecule recoiling from the surface. If the energy channelled to internal motions of the products is large enough, subsequent unimolecular dissociation is possible, and this can be used in mass spectrometric analysis of molecules such as cholesterol [10].

Some effort has been devoted to developing a theoretical description of the ionization of hyperthermal beams on solid surfaces. Empirical modelling based on experimental results has been used to derive a functional form for the fraction of molecules that are ionized by impact with solid surfaces as a function of the initial kinetic energy and the surface temperature [11, 12]. More complete models have tried to address the electron transfer step necessary for ion formation as well as the probability distribution for energy loss in the hyperthermal gas-phase species due to electrostatic interactions of the nascent ion with its image charge in the surface [13]. More refined aspects of the electron transfer mechanism, considering the coupling of electronic states of the hyperthermal projectile and states of the substrate, have been studied [14]. More specifically, collisions of N atoms with an alkali-covered aluminium surface were shown to give rise to non-adiabatic transitions between the states of the projectile and those of the surface.

The ionization and dissociation of I_2 molecules in collisions with a diamond surface have been studied using a semiclassical fewest-switches surface-hopping method [15]. The suitability of this method was verified through comparison of the semiclassical results with exact quantum calculations for a one-dimensional two-state model. Larger-dimensionality calculations using the surface-hopping method indicate that the dependence of the ionization probability on the incident collision energy is not exclusively due to the charge-transfer process. Energy transfer to surface modes was shown to limit the extent of ionization and dissociation. The microscopic mechanism for production of I_2^- ions in this system was analysed through non-adiabatic quantum dynamics calculations [16] by fitting experimental data to adjustable parameters of the theoretical model.

1.2. *Inelastic scattering*

Notwithstanding the large energy involved in hyperthermal processes, if the gas-phase species impinging on surfaces are non-reactive and electron transfer is not favoured, only *inelastic scattering* is produced. Noble gases are perfect candidates to study energy transfer mechanisms at hyperthermal energies due to their inert nature and their large ionization potential and electron affinity, which inhibit reactivity and ionization at moderate energies. Inelastic collisions of hyperthermal noble gases and semiconductors were studied at Bell Laboratories using molecular-beam experiments and trajectory calculations [17–23]. Approximate calculations have been used to estimate the energy transfer in He collisions with LiF surfaces at $\sim$1 eV [24]. Trajectory calculations using an *ab initio*-based interaction potential were used to study the surface site-dependent energy transfer

in Ar collisions with a Pt(111) surface for collision energies of up to 30 eV [25]. The differences in the energy transfer and its consequences for sputtering have been studied in collisions of heavy atoms (Xe and Kr) or light atoms (He and Ne) with a Ni(100) surface by means of the trajectory method and considering energies of up to 500 eV [26]. Analogous calculations on energy transfer and sputtering have been applied to study hyperthermal rare-gas scattering on a Cu crystal [27].

Noble-gas hyperthermal molecular beams have also been directed to softer surfaces, such as organic liquids, alkanethiolate self-assembled monolayers or ice. The Nathanson group has performed experimental studies of noble-gas scattering with liquids. Xe, Ar and Ne were scattered from squalane and perfluoropolyether [28–33]. Simulations in which the structure of the liquid hydrocarbon surface was not explicitly considered were performed to compare with these experiments [34]. Scattering of Ar on liquid indium has been simulated using classical trajectory simulations [35]. The interaction potential between Ar and In atoms was described using a Lennard–Jones potential derived from experiments, while the interaction between indium atoms was treated using an embedded-atom type potential.

Experiments using Ar have been recently carried out using pristine and functionalized alkanethiolate self-assembled monolayers (SAM's) in the Morris group at Virginia Tech. In these sets of experiments study of the influence of the hydrogen-bonding interactions between the chains of modified SAM's on the product translational energy distributions has demonstrated the correlation between dynamics properties and surface structure [36–40]. The Sibener group has also measured energy transfer in inelastic collisions of noble gases with self-assembled monolayers [41, 42]. Detailed simulations of noble-gas scattering on SAM's have been done by the Hase group using the classical trajectory method and accurate potential energy surfaces derived from high-quality *ab initio* calculations [43–47]. Experiments [48] and molecular dynamics simulations [49] of adsorption and trapping of Xe on ice have been recently reported. Collisions of Ar with ice at energies up to 2 eV have been developed using the TIP4P model to describe the interactions between the water molecules and a Lennard–Jones potential for the Ar–H_2O interactions [50]. The large trapping times for Ar and efficient energy transfer suggests that an ice surface behaves more closely to a 'soft' hydrocarbon self-assembled monolayer surface than to a 'hard' metal surface.

Inelastic scattering of hyperthermal species other than noble gases impinging on a variety of surfaces has also been characterized by molecular-beam techniques. Examples of this include Cl_2 on Ag(111) [51] and Si(100) surfaces [52], NO on Pt(111) [53–55], F atoms on fluorinated silicon surfaces [56], CH_4 on Pt(111) [57], or HCl on MgO(100) [58]. The sticking probability of HCl [59–61] and CO [62–64] to ice surfaces has been calculated by Kroes and coworkers. Classical trajectories are used in all of these studies. The TIP4P model for water is used to describe the ice structure, and the HCl and CO interaction with the water molecules on the ice surface are described using pair potentials that reproduce *ab initio* calculations.

Apart from the classical trajectory simulations mentioned above, hyperthermal classical trajectory simulations of energy dissipation into the solid substrate following hyperthermal collisions of noble gases on metal surfaces have also been developed by Zeiri and Lucchese [65]. Combined quantum–classical molecular dynamics treatments in which some of the vibrational degrees of freedom are treated

using a semiclassical approach have recently been developed to describe the collision of a gas-phase molecule with a surface [66].

1.3. *Adsorption*

Although inelastic processes and surface-induced ionization are an important fraction of the possible events in gas/surface hyperthermal collisions, processes in which bonds are broken or formed are of great importance in a number of different fields. The first process that may occur when a gas-phase species approaches a surface with a significant amount of energy is *adsorption*. At hyperthermal energies, the initial collision energy might be large enough that transfer to internal degrees of freedom of the impinging gas-phase molecule can lead to breakage of some of its bonds, providing radical sites for adsorption. This is known as *dissociative adsorption* or *dissociative chemisorption* [67]. Dissociative adsorption of H_2 molecules and isotopic derivatives on metal surfaces is probably the best-studied case due to its interest in heterogeneous catalysis. Early attempts to characterize this process at a theoretical level were reviewed by Darling and Holloway [68]. However, interest in doing theoretical calculations on this system remains unabated, and state-of-the-art quantum dynamics [69, 70] and electronic structure calculations [71, 72] have been carried out very recently.

Dissociative adsorption of CH_4 on a Pt(111) surface has been characterized by spectroscopic detection of CH_3 fragments on the surface after collision, by detection of C–C bond formation in the surface due to diffusion of adsorbed CH_3 moieties [73, 74], and by molecular-beam time-of-flight analysis [75]. Theoretical understanding of this process has been provided by electronic structure determination of the barrier for dissociative adsorption of CH_4 on Ni(111) [76] and by analytic models that relate reactive probability to the kinetic energy, angle of incidence and surface corrugation [77]. More detailed simulations of dissociative chemisorption of CH_4 on Ni(111) have used the classical trajectory method with an empirical potential energy surface [78] and approximate two-dimensional quantum dynamics calculations on an *ab initio*-derived surface [79]. Although density functional calculations have been performed to characterize the preferential sites for adsorption of short-chain alkanes on Pt(111) [80], and Monte Carlo simulations of the rate of ethane dissociation on Pt(111) have been reported [81], detailed molecular dynamics simulations of alkane + Pt(111) hyperthermal collisions are still needed.

Molecular-beam studies of the dissociative adsorption of Si_2H_6 on Si(100) and Si(111) surfaces [82] have been complemented with classical trajectory calculations of SiH_3 radical deposition on hydrogenated Si(100) surfaces [83]. This, and other classical trajectory studies of the adsorption of gas-phase Si, C and H-containing species on Si, C and H-containing surfaces, have been possible due to the development of a reactive bond-order many-body empirical potential for these species. The original work by Tersoff [84] was followed and extended by Brenner and coworkers, who generated an analytic potential energy surface for Si, C and H-containing systems that has become very popular [85–87]. Examples of use of these potentials for study of adsorption at hyperthermal energies include: Si and C deposition on a SiC(0001) surface [88] and methyl [89, 90] and acetylene [91] adsorption on a diamond (001) surface.

Carter and coworkers [92] performed *ab initio* molecular dynamics studies of collisions of F_2 molecules with clean and partially fluorinated Si(100) surfaces

at up to 4 eV collision energies. The differences between two *ab initio*-derived potential energy surfaces for this system were studied by Schoolcraft *et al*. for collision energies up to 1.67 eV [93]. *Ab initio* molecular dynamics calculations have also been used to simulate the dynamics of dissociative chemisorption of Cl_2 molecules striking a Si(111)–(2x1) surface at $E_{coll} = 1$ eV [94].

One of the principal applications of hyperthermal dissociative adsorption or chemisorption is crystal growth. Crystal growth is the process whereby molecular species interacting with a surface at hyperthermal energies are incorporated to the surface without significant degradation of the solid substrate [95]. For example, epitaxial Si and Ge- or Sb-doped Si alloys have been grown on Si(001) surfaces through irradiation of the solid substrates with Si, Ge and Sb molecular beams having energies of about 15 eV [96, 97]. Recently, it has been shown that growth of highly ordered organic films using hyperthermal molecular beams is also possible [98]. Early models of crystal growth from collisions of hyperthermal species on surfaces were developed by Lifshitz and coworkers [99]. Molecular dynamics simulations of crystal growth from collisions of organic molecules on diamond have been carried out using the above-mentioned empirical bond-order potential for hydrocarbons [100–103]. Deposition of hyperthermal metallic atoms has also been studied with molecular dynamics simulations that used empirical embedded-atom models to account for the internuclear potentials [104, 105]. Although the previous examples are all atomistic molecular dynamics simulations, kinetic Monte Carlo methods have likely been the most used technique to study crystal growth [106–111].

1.4. *Etching*

Another application of the effects of hyperthermal collisions of gas-phase species on solid surfaces is chemical etching, erosion and sputtering [112]. These processes occur when gas-phase molecules impinging on surfaces induce bond breakage in the condensed-phase substrate with subsequent surface mass loss [113]. Conventional plasma processing of materials usually involves ionic beams. However, the presence of ions might jeopardize the electronic properties of semiconductor materials, and therefore ionic etching must be avoided for these materials. Considerable effort has therefore been put into generating neutral beams at hyperthermal energies. An example of success in this direction has been the production of stable atomic fluorine beams [114–117].

From a theoretical perspective, the Garrison group has led the way in the simulation of processes occurring at surfaces that result in degradation. We refer the reader to extensive reviews of this work already extant in the literature [118–120].

Other molecular dynamics simulations of etching have been reported. The reactions of fluorine atoms with fluorinated silyl derivatives have been studied using a potential derived from *ab initio* calculations [121]. Details of the electronic structure of collisions of hyperthermal Cl_2 molecules with a Si(100) surface and calculated using density functional theory have recently been reported [122]. Molecular dynamics simulations have been used to study the chemical sputtering of carbon with hyperthermal deuterium, such as is important in divertor materials in tokamats [123].

1.5. *Collision-induced dissociation*

Collision-induced dissociation (CID) is the process whereby a molecule colliding with an atom, molecule or surface dissociates as a consequence of the collision. Early calculations on gas-phase atom + diatom CID were developed using quasiclassical trajectories [124–130]. For a review on these early studies see Ref. [131]. Although quasiclassical trajectory calculations of CID in atom + diatom collisions have also been carried out in recent time [132], the progress in computational capabilities and the development of efficient algorithms have allowed semiclassical [133–135] and quantum dynamics calculations to be performed for a number of lightweight triatomic reactions [136–143]. Some progress in tetratomic collisions has also been made. The most studied system has been $H_2 + H_2$ in which both quasiclassical trajectories [144–146] and quantum scattering [147–149] calculations have been developed. Bowman [150] and Light [151] also studied CID in Ar + HCO collisions using QM methods.

Beyond four atoms, the general unavailability of reliable potential energy surfaces has inhibited the development of many CID studies. The reactions of ground-state carbon atoms with alkanes have been reviewed recently [152]. Hase carried out calculations of the dissociation of metal clusters by rare-gas impact [153, 154]. CID of water dimers by hyperthermal collisions with He has been studied using quasiclassical trajectories [155].

1.6. *Surface-induced dissociation*

The particular case of collision-induced dissociation of a gas-phase molecule after collision with a surface is often termed *surface-induced dissociation* (SID) [156]. Early studies on this have been reviewed by Kleyn [157]. More recently, there has been a variety of studies of dissociation of hyperthermal neutral species by collision with surfaces. Dissociation of *n*- and *i*-C_3F_7NO molecules impinging on crystalline MgO(100) [158, 159], GaAs(100) and Ag(111) [160] surfaces has been characterized by analysis of the recoiling NO products. NO detection has also been used to prove dissociation of vibrationally excited NO_2 colliding at hyperthermal energies with MgO(100) [161, 162].

A particular case of collision-induced dissociation is that in which the species that undergoes dissociation is initially coordinated to the surface. Dissociation occurs when a non-reactive hyperthermal projectile (such as a noble gas) aimed at the surface breaks bonds in the adsorbed species [163–165].

1.7. *Collision-induced desorption*

Collision-induced desorption is the process whereby a chemical species physisorbed or chemisorbed on a solid surface is desorbed upon collision with an impinging gas-phase species. Experimental examples of this that have used hyperthermal beams include desorption of physisorbed Xe atoms on Pt(111) by hyperthermal collisions with Ar atoms striking the surface [166], desorption of methane on a Ni(100) surface by Ar [167], desorption of silicon fluorides from a fluorinated Si(100) surface induced by hyperthermal Xe atoms [168], desorption and dissociation of O_2 molecules chemisorbed on Ag(100) [169, 170] and Ag(110) [171] by hyperthermal rare gases collisions, N_2 desorption from Ni(100) by hyperthermal Xe atoms [172], desorption of alkanethiols [173] and alkane molecules [174] from Au(111) by Xe atoms, as well as desorption of N_2 molecules from Ru(001) by hyperthermal Ar and Kr [175]. Classical dynamics calculations

on collision-assisted desorption of molecules have been developed by Zeiri and coworkers [176, 177] and by the Hase group [178]. Customarily, these calculations are based on classical trajectory simulations propagated on potential surfaces that contain *ab initio* information. For a recent review see Ref. [179].

More exotic phenomena associated with the effect of hyperthermal collisions between noble gases and species adsorbed on solid surfaces include collision-induced adsorption of species that are initially in the surface to positions well below the surface (subsurface implantation) [180, 181] or diffusion of physisorbed molecules on a surface induced by bombardment with hyperthermal noble gases [182].

After reviewing research on hyperthermal neutral scattering, in the following we discuss the low Earth orbit problem and its relationship with hyperthermal chemistry.

2. Materials erosion in low earth orbit

Degradation of materials on the surface of satellites and spacecraft operating in low Earth orbit (LEO) was discovered long ago [183, 184] and vigorous research has been conducted to investigate its origin and possible mitigation ever since. A number of experimental efforts have been directed at simulating the LEO environment in the laboratory. It is well-known that the most abundant species in the 200–700 km altitude range is atomic oxygen in its ground state [185]. The large velocity of a spacecraft in low Earth orbit (e.g. one complete orbit of the *International Space Station* around the Earth takes ~90 min) gives rise to a collision energy between oxygen atoms in the LEO atmosphere and the exposed spacecraft surfaces of about 5 eV. Therefore, a number of experiments have studied the interactions of hyperthermal atomic oxygen with polymeric surfaces.

Early studies of the erosion of hydrocarbon polymers with different hydrogen content and structure by $O(^3P)$ were reviewed by Kleiman and coworkers [186]. Several hydrocarbon polymers with different fluorine content have been exposed to 5 eV atomic oxygen [187]. Erosion of polyimide polymers has been thoroughly characterized [188–191], and the rate of erosion of Kapton® is commonly used as a standard for calibration of the erosion of other polymers. Recent interest in graphite erosion by atomic oxygen has led to the development of very refined experiments [192–194], which are being complemented with electronic structure and kinetic Monte Carlo simulations [195]. The experimental work on polymer erosion by $O(^3P)$ has been recently reviewed by Minton and Garton [196].

Inorganic surfaces, such as Si(100) [197–199], silica [200], and polyhedral oligomeric silsesquioxane-based composites [201, 202], have also been exposed to hyperthermal oxygen atoms. Commonly, exposure of silicon surfaces to atomic oxygen leads to oxidation of the surface. This results in the formation of an exterior silica layer that passivates the underlying surface, protecting it from subsequent attack by hyperthermal atomic oxygen. The ability of hyperthermal oxygen to produce oxidation has been investigated using metallic and semiconductor surfaces [203–206].

The availability of well-characterized beams of hyperthermal atomic oxygen has enabled a variety of studies to be done that have revealed several phenomena occurring when $O(^3P)$ collides with solid surfaces. Analysis of atomic oxygen scattered from metal surfaces [207] and liquid hydrocarbons [208] has provided information about the dynamics of inelastic scattering at hyperthermal energies

and its dependence on surface structure. Atomic-oxygen collision-induced desorption of NO from metal surfaces [209] and collision-induced desorption of CO and CO_2 from polystyrene and polyimide by hyperthermal N_2 and Ar [189] have also been studied.

In contrast with this wealth of experimental studies, detailed numerical simulations of the interaction of hyperthermal $O(^3P)$ with materials are clearly lacking. While empirical potentials have been used in molecular dynamics simulations of $O(^3P)$ with graphite [210], high-accuracy first-principles molecular dynamics simulations of $O(^3P)$ reactions with graphite and carbon nanotubes have only recently been used to study morphological features of oxygen insertion and doping in graphitic materials [211]. Quantum mechanical calculations have also been used to describe the possibility of C–C breakage by $O(^3P)$ in gas-phase alkanes [212, 213].

3. Reactions of $O(^3P)$ with short-chain alkanes in the gas phase

We have recently been interested in modelling the microscopic mechanisms for materials degradation in low Earth orbit at the molecular level, especially mechanisms associated with hyperthermal atomic oxygen. Our approach has been to study the electronic structure details of the interaction potential between $O(^3P)$ and short-chain alkanes, and to simulate collisions at hyperthermal energies using molecular dynamics simulations [214–217].

The reasons for our choice of short-chain gas-phase alkanes as a starting point towards a detailed molecular-level understanding of erosion in LEO are manifold. Hydrocarbon-based polymers have been used as coatings of spacecraft operating in LEO. The detection of erosion of these polymers in orbit subsequently triggered ground-based experimental studies that have provided a wealth of data on the degradation of a number of hydrocarbon polymers under the action of $O(^3P)$. Recently, experimental measurements of the $O(^3P)$ + methane, ethane and propane reactions have been carried out by Minton and coworkers [214, 217] using a well-characterized hyperthermal atomic oxygen source [218]. This new set of data complements existing information on the gas-phase reactions of $O(^3P)$ with alkanes at near-thermal collision energies [219, 220].

Collisions of $O(^3P)$ with gas-phase alkanes also serve as an intermediate step towards the development of gas/surface studies. From a theoretical perspective, accurate atomistic simulations of gas/surface chemical reactions are daunting. Usually, the large number of reactive channels that contribute to the overall erosion process inhibits development of analytical potential energy surfaces. Therefore, the only possible way to develop reliable molecular dynamics simulations of collision processes is through direct dynamics, a technique in which the potential energy and gradients needed are evaluated quantum mechanically (QM) at each point along the trajectories. However, this is computationally unwieldy because the number of atoms involved in the collision process is very large, and the computation time required to carry out accurate quantum mechanical calculations scales exponentially with the number of electrons.

One of the approaches to perform classical trajectory simulations of gas/surface collisions with quantum mechanical gradients is to use approximate QM methods, such as semi-empirical Hamiltonians. However, these cheap QM methods have to be used with caution, as they often fail to properly describe fundamental aspects of the electronic structure of the system under consideration.

Our strategy to simulate gas/surface $O(^3P)$-polymer collisions has been based on the use of a semi-empirical Hamiltonian of limited accuracy, but which adequately reproduces the main features of the potential energy surfaces. Prior to doing gas/surface studies, we calibrated the performance of several semi-empirical Hamiltonians in the reactions of $O(^3P)$ with short-chain alkanes in two ways. First, we compared the properties of the stationary points of the reaction pathways accessible under hyperthermal conditions with benchmark high-accuracy QM calculations, and second, we carried out reaction dynamics studies by means of the classical trajectory method to compare with extant experimental or higher-level theoretical data. Aside from assessing the suitability of semi-empirical Hamiltonians for ensuing gas/surface studies, the gas-phase studies allowed us to derive a wealth of information about the microscopic mechanisms of the interactions of hyperthermal $O(^3P)$ with hydrocarbons and their implication in low Earth orbit erosion.

3.1. *Electronic structure calculations*

There are three primary reaction channels in collisions of $O(^3P)$ with alkanes at hyperthermal energies:

$$O(^3P) + C_nH_{2n+2} \rightarrow OH + C_nH_{2n+1} \qquad \text{(H abstraction)}$$

$$O(^3P) + C_nH_{2n+2} \rightarrow H + OC_nH_{2n+1} \qquad \text{(H elimination)}$$

$$O(^3P) + C_nH_{2n+2} \rightarrow OC_mH_{2m+1} + C_{(n-m)}H_{2(n-m)+1} \qquad \text{(C} - \text{C breakage)}$$

H abstraction generates an OH radical and an alkyl radical. In H elimination processes, O adds to the hydrocarbon chain and generates an alkoxy radical after ejection of a hydrogen atom. C–C breakage processes generate both an alkyl radical and an alkoxy radical. In addition to these primary processes, secondary reaction channels are possible. Abstraction of a hydrogen atom by the OH radical generated in the H abstraction reaction gives rise to H_2O and a triplet hydrocarbon diradical. If the alkoxy radicals produced in H elimination processes contain a large amount of internal energy as a consequence of the reactive event, elimination of a second hydrogen atom is possible with formation of an aldehyde or ketone. Secondary H eliminations are also possible in the radicals generated in C–C breakage reactions.

Tables 1–3 show reaction energies and barriers for H abstraction, H elimination and C–C breakage processes, respectively, for the $O(^3P) + C_nH_{2n+2}$ ($n = 1, 2, 3$) reactions. Schematic representations of the corresponding reaction coordinates and saddle-point structures are displayed in figure 1 for $O(^3P) + CH_4$ and in figure 2 for $O(^3P) + C_2H_6$. In the reactions of $O(^3P)$ with propane, we distinguish between reactions that involve primary or secondary sites. Figure 3 is for reactions involving the methyl ends of the propane molecule (primary carbon atoms) and figure 4 is for reactions taking place on the central methylene unit. Figure 5 displays the geometries of some of the products and saddle points involved in the $O(^3P) + C_3H_8$ reactions.

The lowest barrier process is H abstraction to generate OH plus an alkyl radical. Experimental thermal rate constants for all three reactions have been available for a long time [221, 222]. Product properties—in particular, OH internal state distributions—have also been measured with $O(^3P)$ having initial translational energies slightly above room temperature. This has been recently reviewed by

Table 1. Calculated reaction energy and barrier heights for the H abstraction reactions $O(^3P) + C_nH_{2n+2} \rightarrow OH + C_nH_{2n+1}$, with $n = 1$, 2, and 3.

H abstraction, $O(^3P) + C_nH_{2n+2} \rightarrow OH + C_nH_{2n+1}$					
Reaction energy/eV					
	$O(^3P) + CH_4 \rightarrow OH + CH_3$	$O(^3P) + C_2H_6 \rightarrow OH + C_2H_5$	$O(^3P) + C_3H_8 \rightarrow OH + n\text{-}C_3H_7$	$O(^3P) + C_3H_8 \rightarrow OH + n\text{-}C_3H_{7\prime}$	$O(^3P) + C_3H_8 \rightarrow OH + i\text{-}C_3H_7$
MSINDO	−0.342	−0.771	−0.748	−0.761	−1.102
B3LYP[a]	0.001	−0.221	−0.200	−0.176	−0.370
CCSD(T)[b]	0.246	0.085	0.118	0.105	−0.010
MRCI + Q	0.061[c]	−0.061[d]			
Reaction barrier/eV					
	TS1M	TS1E	TS1P	TS1P′	TS2P
MSINDO	0.564	0.370	0.359	0.353	0.243
B3LYP[a]	0.174	0.026	−0.016	−0.008	−0.114
CCSD(T)[b]	0.633	0.460	0.463	0.449	0.333
MRCI + Q	0.455[c]	0.390[d]			

[a] B3LYP/6-311 + + G** calculations.
[b] CCSD(T)/6-311 + + G** single-point calculations using geometry and frequencies obtained in UMP2/6-311G** calculations.
[c] MRCI + Q(10,10) calculations with complete basis set extrapolation using geometry and frequencies obtained in CASPT2(10,10)/cc-pVTZ calculations [223].
[d] MRCI + Q(8,8) calculations with complete basis set extrapolation using geometry and frequencies obtained in CASPT2(8,8)/cc-pVTZ calculations [223].

Table 2. Calculated reaction energy and barrier heights for the H elimination reactions $O(^3P) + C_nH_{2n+2} \rightarrow H + OC_nH_{2n+1}$, with $n = 1$, 2, and 3.

H elimination, $O(^3P) + C_nH_{2n+2} \rightarrow H + OC_nH_{2n+1}$									
Reaction energy/eV									
	$O(^3P) + CH_4 \rightarrow H + OCH_3$	$O(^3P) + C_2H_6 \rightarrow H + OC_2H_5$	$O(^3P) + C_3H_8 \rightarrow H + n\text{-}OC_3H_7$	$O(^3P) + C_3H_8 \rightarrow H + n\text{-}OC_3H_{7\prime}$	$O(^3P) + C_3H_8 \rightarrow H + i\text{-}OC_3H_7$				
MSINDO	0.081	−0.285	−0.208	−0.235	−0.493				
B3LYP[a]	0.568	0.401	0.400	0.314	0.224				
CCSD(T)[b]	0.891	0.657	0.654	0.612	0.476				
Reaction barrier/eV									
	TS2M	TS3M	TS2E	TS3E	TS3P	TS3P′	TS4P	TS5P	TS6P
MSINDO	1.867	1.990	1.701	1.671	1.861	1.761	1.764	1.847	1.513
B3LYP[a]	1.781	2.140	1.814	2.019	1.902	1.794	2.014	1.871	1.978
CCSD(T)[b]	2.578	2.743	2.315	2.585	2.393	2.283	2.565	2.344	2.501

[a] B3LYP/6-311 + + G** calculations.
[b] CCSD(T)/6-311 + + G** single-point calculations using geometry and frequencies obtained in UMP2/6-311G** calculations.

Table 3. Calculated reaction energy and barrier heights for the C–C breakage reactions $O(^3P) + C_nH_{2n+2} \rightarrow C_mH_{2m+1} + OC_{(n-m)}H_{2(n-m)+1}$, with $n = 2$ and 3.

C–C breakage, $O(^3P) + C_nH_{2n+2} \rightarrow C_mH_{2m+1} + OC_{(n-m)}H_{2(n-m)+1}$			
Reaction energy/eV			
	$O(^3P) + C_2H_6 \rightarrow CH_3 + OCH_3$	$O(^3P) + C_3H_8 \rightarrow CH_3 + OC_2H_5$	$O(^3P) + C_3H_8 \rightarrow C_2H_5 + OCH_3$
MSINDO	−0.720	−0.930	−0.994
B3LYP[a]	−0.262	−0.326	−0.381
CCSD(T)[b]	0.208	0.135	0.210
MRCI + Q[c]	0.048		
Reaction barrier/eV			
	TS4E	TS5E	TS7P	TS8P
MSINDO	1.645	2.031	1.773	2.054
B3LYP[a]	1.574	2.183	1.676	2.120
CCSD(T)[b]	2.169	2.742	2.259	2.667
MRCI + Q[c]	2.033			

[a] B3LYP/6-311 + + G** calculations.
[b] CCSD(T)/6-311 + + G** single-point calculations using geometry and frequencies obtained in UMP2/6-311G** calculations.
[c] MRCI + Q(8,8) calculations with complete basis set extrapolation using geometry and frequencies obtained in CASPT2(8,8)/cc-pVTZ calculations [223].

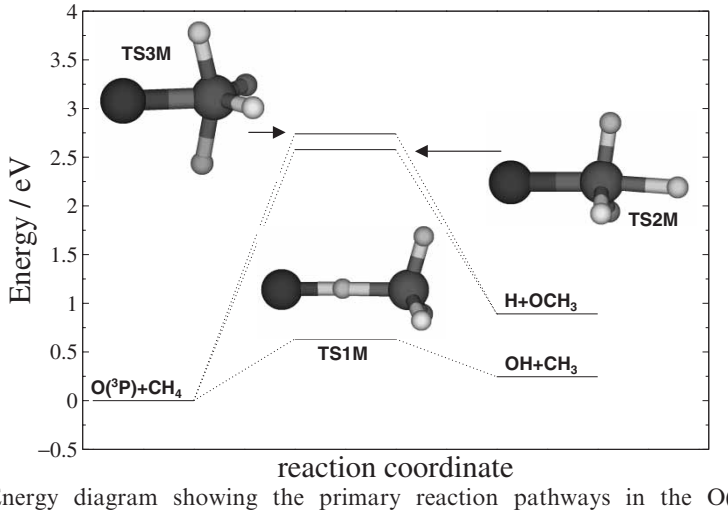

Figure 1. Energy diagram showing the primary reaction pathways in the $O(^3P) + CH_4$ system. The energies correspond to CCSD(T)/6-311 + + G** calculations. The geometries of the saddle points depicted in the figure correspond to UMP2/6-311G** calculations.

Ausfelder and McKendrick [220]. Numerous theoretical calculations of the $O(^3P) + CH_4 \rightarrow OH + CH_3$ reaction energy and barrier have been carried out over the years. Hase and coworkers have recently reviewed these theoretical efforts, and have developed the most rigorous calculations of the $O(^3P) + CH_4 \rightarrow OH + CH_3$

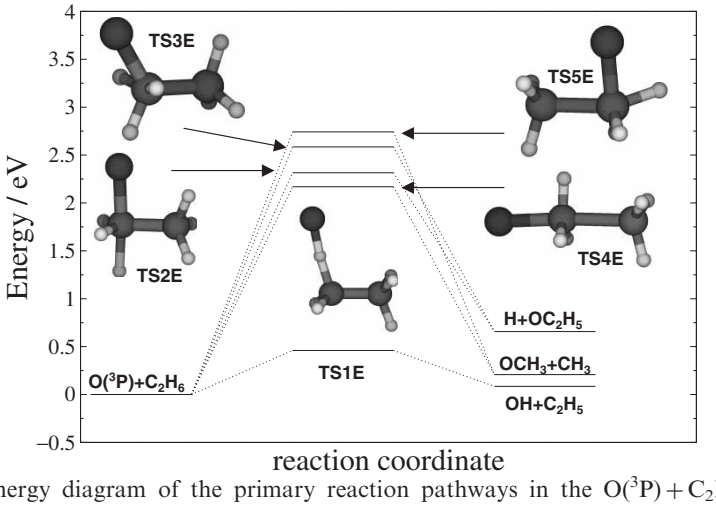

Figure 2. Energy diagram of the primary reaction pathways in the $O(^3P) + C_2H_6$ system. The energies correspond to CCSD(T)/6-311++G** calculations. The geometries of the saddle points depicted in the figure correspond to UMP2/6-311G** calculations.

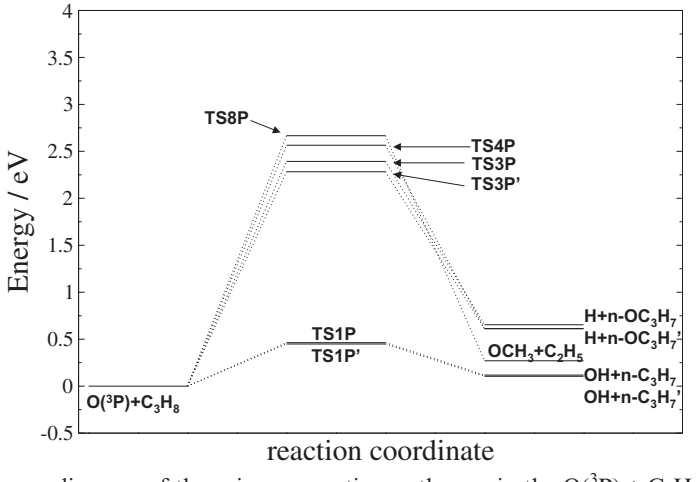

Figure 3. Energy diagram of the primary reaction pathways in the $O(^3P) + C_3H_8$ system that involve primary C atoms. The energies correspond to CCSD(T)/6-311++G** calculations.

and $O(^3P) + C_2H_6 \rightarrow OH + C_2H_5$ reaction energetics to date [223]. They used multireference configuration interaction theory with single, double, and quadruple excitations (through the Davidson correction) with complete basis set extrapolation (MRCI+Q/CBL). These single-point energy calculations were performed at geometries calculated using CASSCF or CASSPT2 wavefunctions and triple-zeta basis sets.

Table 1 shows these results, in comparison with lower-level calculations that use the B3LYP hybrid functional of density functional theory (DFT) with the 6-311++G** basis set and single-reference coupled-cluster calculations with single, double, and perturbative triple excitations (CCSD(T)) with the same basis

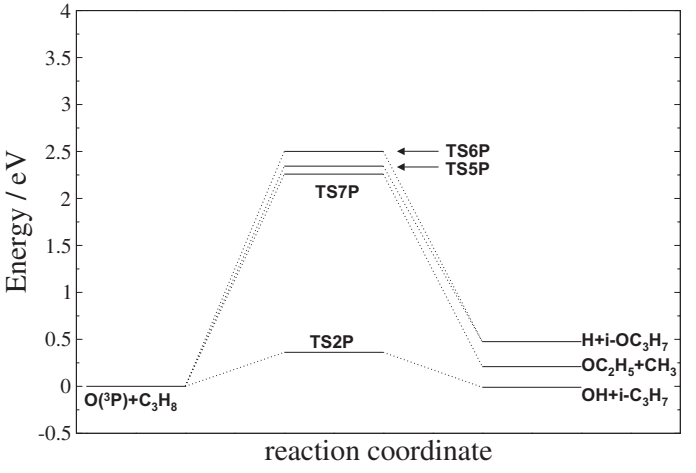

Figure 4. Energy diagram of the primary reaction pathways in the $O(^3P) + C_3H_8$ system that involve secondary C atoms. The energies correspond to CCSD(T)/6-311++G** calculations.

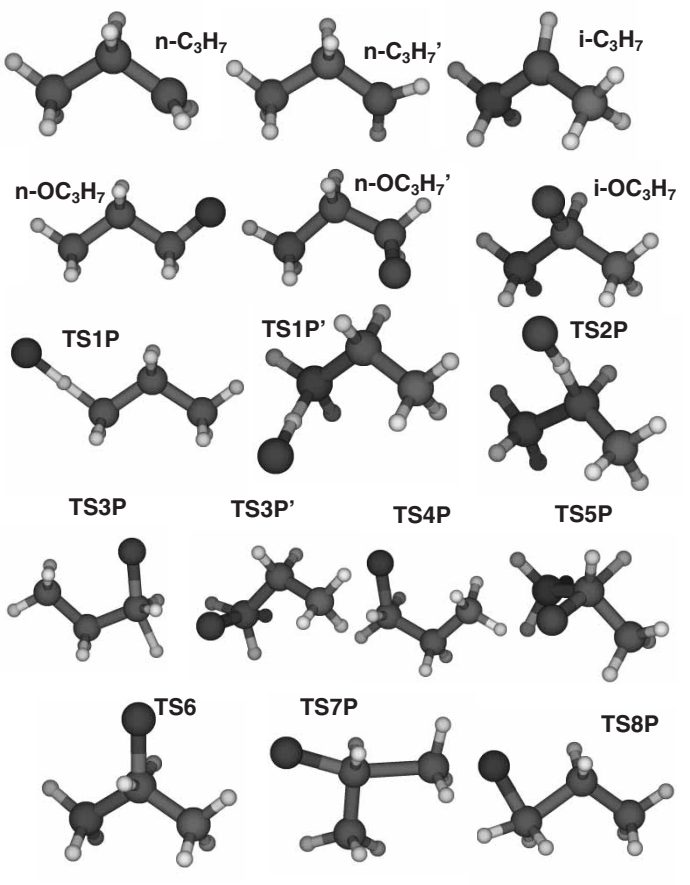

Figure 5. Structure of saddle points and products in the $O(^3P) + C_3H_8$ system. The geometries correspond to UMP2/6-311G** calculations.

set as the DFT calculations. The CCSD(T) single-point calculations are performed on structures optimized at the UMP2/6-311G** level. The table also shows the results of the MSINDO semi-empirical Hamiltonian [224]. These results are important because MSINDO has been used in the classical trajectory studies of the $O(^3P)$ collisions with hydrocarbons at hyperthermal energies that we review in the next section. It is noticeable that in all cases the B3LYP and CCSD(T) results provide lower and upper bounds to the more accurate MRCI + Q calculations, respectively. This will be important to establish estimates in systems in which the higher-accuracy calculations are not feasible.

The H abstraction reactions are approximately thermoneutral. However, the reactions become more exothermic with increasing chain length. This can be seen comparing the H abstraction reaction energies in the reactions with CH_4 and C_2H_6. There are three different abstraction sites in C_3H_8. We denote by *n*-C_3H_7 the propyl radicals produced in H abstractions from the terminal methyl groups, and by *i*-C_3H_7 the propyl molecule in which the radical is in the secondary C atom. There are two possible *n*-C_3H_7 radicals. One is produced after abstraction of the H atom that is in the carbon backbone plane, and has C_s symmetry. Abstraction of the out-of-plane terminal hydrogen atoms leads to an asymmetric propyl radical that we denote *n*-C_3H_7'. These three product channels are connected with the reagents through three different saddle points. TS1P leads to *n*-C_3H_8, TS1P′ leads to *n*-$C_3H_{8\prime}$ and TS2P leads to *i*-C_3H_7. The reaction energy of the abstraction reactions of propane leading to terminal propyl radicals (*n*-C_3H_7 and *n*-C_3H_7') are very similar to those of ethane for all of the QM methods used. On the other hand, the OH + *i*-C_3H_7 asymptote is the lowest energy one.

This trend holds for the reaction barriers ($\Delta E^{\ddagger}$): $\Delta E^{\ddagger}$ ($O(^3P) + CH_4 \rightarrow OH + CH_3$) > $\Delta E^{\ddagger}$ ($O(^3P) + C_2H_6 \rightarrow OH + C_2H_5$) ≈ $\Delta E^{\ddagger}$ ($O(^3P) + C_3H_8 \rightarrow OH +$ *n*-C_3H_7) ≈ ΔE ($O(^3P) + C_3H_8 \rightarrow OH +$ *n*-C_3H_7') > $\Delta E^{\ddagger}$ ($O(^3P) + C_3H_8 \rightarrow OH +$ *i*-C_3H_7). It is noticeable that all of the methods examined are able to reproduce this behaviour.

Table 2 shows the energetics of the H elimination reaction. Formation of H plus an alkoxy radical is endothermic by about 0.5 eV. The alkoxy radicals are more stable for longer hydrocarbon chains. In the case of propane, elimination in the primary carbon atoms is energetically less favoured than generation of *i*-propoxy. This concurs with the trends observed in H abstraction reactions.

H elimination can proceed through more than one first-order saddle point. The lowest-energy saddle point is ~2 eV above reagents. This large reaction barrier explains why this channel had not been detected in earlier near-thermal experiments. Initial studies of $O(^3P)$ + alkane reactions were devoted to kinetics and dynamics properties at thermal or combustion energies. Under these conditions, the H elimination channel is closed. The recent interest in the characterization of reactions of $O(^3P)$ at hyperthermal energies, such as are important to LEO erosion, have spurred a thorough characterization of this reaction channel. In the reactions with CH_4 and C_2H_6 the structures of the lowest-energy H elimination saddle point are reminiscent of the SN2 reaction mechanism from organic chemistry (or more precisely SH2, for substitution homophilic second order, as the reaction does not involve Lewis acid–base interactions). The C–O bond that is being formed is nearly collinear with the C–H bond that is being broken (see insets of figures 1 and 2). The higher-energy first-order saddle points located in the reactions with CH_4 and C_2H_6 (TS3M and TS3E, respectively) are ~0.3 eV more energetic than the

lowest-energy ones (TS2M and TS2E). The structure of these higher-energy saddle points is characterized by the formation of a C–O bond and the symmetric elongation of two C–H bonds that are nearly perpendicular to the C–O bond. Based on the saddle-point structure, one might imagine that this saddle point would lead to double H atom elimination; however, our calculations of the minimum-energy reaction path toward products indicate that only one of the two C–H bonds that are stretched in the saddle point dissociates, while the other contracts to the equilibrium distance in the alkoxy radical.

Several saddle points for H elimination have been located in the $O(^3P) + C_3H_8$ reaction. TS3P and TS3P′ are the SN2-like H elimination saddle points in the terminal methyl groups, while TS4P is a higher-energy saddle point also in a primary C atom. TS5P and TS6P are an SN2-like and higher-energy saddle point in the central methylene unit of propane, respectively.

Table 3 presents reaction energies and barriers for C–C breakage processes in the $O(^3P) + C_2H_6$ and C_3H_8 reactions. $O(^3P)$ can break C–C bonds in propane yielding two different products: $CH_3 + OC_2H_5$ and $OCH_3 + C_2H_5$. These reactions are near-thermoneutral. As with H elimination, two different reaction pathways connect reagents and C–C breakage products. The lower-energy saddle-point energies for both reactions (TS4E and TS7P) are in the vicinity of 2 eV above the reagents, while an additional ~0.5 eV is needed to surmount the higher-energy saddle points (TS5E and TS8P). The geometries of the lower-energy C–C breakage saddle point in the reaction with both ethane and propane are similar, with the O–C bond being formed near-collinearly to the C–C bond that is being broken. These saddle points also represent a process analogous to an SN2 reaction, where the exit group in this case is CH_3. The higher-energy (TS5E and TS8P) saddle points can be described as O insertion into a C–C bond. Insertion mechanisms are archetypal of electronically (singlet) excited oxygen atoms ($O(^1D)$). However, these results indicate that ground-state (triplet) atomic oxygen also undergoes insertion in C–C bonds at hyperthermal energies. Occasionally, and depending on the electronic structure method used, we have found that the minimum-energy reaction paths starting from the saddle points TS5E and TS8P lead to H elimination products rather than CH_3 elimination.

Summarizing, electronic structure studies of the interactions of $O(^3P)$ with short-chain alkanes indicate that there are important reaction mechanisms other than the well-characterized low-energy H abstraction to give OH plus an alkyl radical. These novel reaction pathways open up at ~2 eV. A common feature of the saddle points involved in these high-energy processes is the formation of a C–O bond. Concomitant breakage of a C–H bond or a C–C bond gives rise to H elimination products or C–C breakage products, respectively. Both of these processes have deleterious effects on the alkane chains, and thus are important to polymer degradation. H elimination is formally an oxidation process, while C–C breakage induces mass loss and oxidation.

3.2. *Reaction dynamics calculations*

Simulation of collisions of $O(^3P)$ atoms with short-chain saturated alkane molecules at hyperthermal energies has been carried out to gain additional insight into the relative importance and dynamics characteristics of the different reaction pathways described in the previous section. We have performed classical trajectory calculations for the $O(^3P) + CH_4$, C_2H_6 and C_3H_8 reactions at

different collision energies ranging from $E_{coll} = 0.65$ to 6 eV. We considered such a large range of collision energies in order to bridge low-energy and hyperthermal-energy experiments, and to learn how the dynamics properties depend on collision energy.

Our choice of the classical trajectory method to explore the dynamics behaviour of the system is justified for a variety of reasons. The number of atoms in the reactions under consideration is relatively large and well out of the reach of approximate full-dimensional quantum dynamics methods. Reduced-dimensionality methods have proved useful in the study of a variety of polyatomic reactions [225]. However, these calculations have been restricted to low energies, where the number of open states and thereby the size of the rovibrational basis sets required in quantum dynamics calculations are small enough to allow for a timely computation. Also, most reduced-dimensionality methods cannot handle multiple reaction paths. Quantum dynamics calculations become unwieldy at hyperthermal energies. On the other hand, classical trajectory calculations become less expensive at larger collision energy. Additionally, it is well-known that quantum effects decrease with decreasing De Broglie wavelength (h/p, where h is Planck's constant and p is the momentum). Thus, at large collision energies (large momenta) quantum effects are expected to attenuate and the classical approach becomes more valid.

The dynamics behaviour of a system is tied to the potential energy surface. The preceding section illustrates that there is a wealth of processes that can take place when a ground-state oxygen atom strikes an alkane at hyperthermal energies. Reliable molecular dynamics simulations of reactive processes must reasonably describe as many aspects of the potential energy surface as possible. Thus, one of the main difficulties associated with the development of dynamics calculations for $O(^3P)$ + alkane collisions is the need for accurate forces acting on the nuclei during the collision process. The most commonly used approach for force evaluation is to develop analytical potential energy surfaces by fitting high-accuracy *ab initio* data to mutiparameter mathematical functions. However, the grid of *ab initio* data required to cover all of the relevant regions of the surface explored in hyperthermal collisions, and the large number of parameters needed to obtain a function with enough flexibility to reproduce the features of all of the reaction pathways involved while avoiding spurious behaviour, make this process impractical.

Another approach to realistic molecular dynamics simulations is the 'direct dynamics' method. Here, the energy gradients required to propagate the trajectories are obtained from electronic structure calculations 'on-the-fly', i.e. while the trajectory is evolving. This implies several million gradient calculations using electronic structure methods such as the ones described earlier. While millions of *ab initio* or DFT energy gradient calculations imply prohibitive computation times, a quantum mechanical framework is necessarily required to account for as many of the details of bond breakage/formation processes that take place in hyperthermal collisions of $O(^3P)$ with alkanes as possible. Semi-empirical Hamiltonians, having much smaller computation times, are an alternative to first-principles calculations for direct dynamics. However, the approximate nature of semi-empirical Hamiltonians requires careful calibration of their suitability and possible pitfalls prior to the development of reaction dynamics studies. Calculations of the stationary points presented in tables 1–3 were done with the PM3, AM1, and MSINDO semi-empirical Hamiltonians. MSINDO clearly outperformed PM3 and AM1. All of the methods underestimate the reaction energies (see MSINDO values in tables 1–3),

but MSINDO gives much more accurate reaction barriers. The root-mean-square deviation between the MSINDO energies for the 18 saddle points listed in tables 1–3 and the corresponding B3LYP/6-311++G** data is ~0.25 eV. This is reduced to ~0.20 eV for B3LYP/6-31G* calculations. The approximately three-order-of-magnitude difference in computation time between MSINDO and B3LYP/6-31G* calculations led us to carry out extensive direct dynamics calculations using MSINDO. A smaller set of trajectories was run using B3LYP/6-31G* to verify the legitimacy of MSINDO dynamics results.

Batches of ~10,000 trajectories have been calculated for $O(^3P) + CH_4$, C_2H_6 and C_3H_8 at collision energies in the 0.65–6.0 eV range. The integration time-step used in all cases was 10 a.u. Small spin contamination in the MSINDO UHF wavefunction leads to tolerable imperfections in the energy conservation of the order of ~1 kcal/mol. Smaller integration steps do not lead to better energy conservation. Initial conditions for the alkane molecules are sampled from zero-point motion. The trajectories are started (stopped) at ~12 a.u. separation distance between reagents (products).

3.2.1. *Cross-sections*

Cross-sections as a function of collision energy are plotted in figure 6 for $O(^3P) + CH_4$. We distinguish between two primary product channels: H abstraction and H elimination. The H abstraction reaction yields $OH + CH_3$, whereas in the H elimination reaction we have summed the cross-sections for the $OCH_3 + H$ and $OCH_2 + H + H$ products. The $H + OCH_3$ products are the H elimination dominant products at all energies. We do observe double H elimination, but only above $E_{coll} = 3.0$ eV. At $E_{coll} = 6.0$ eV, the $OCH_2 + H + H$

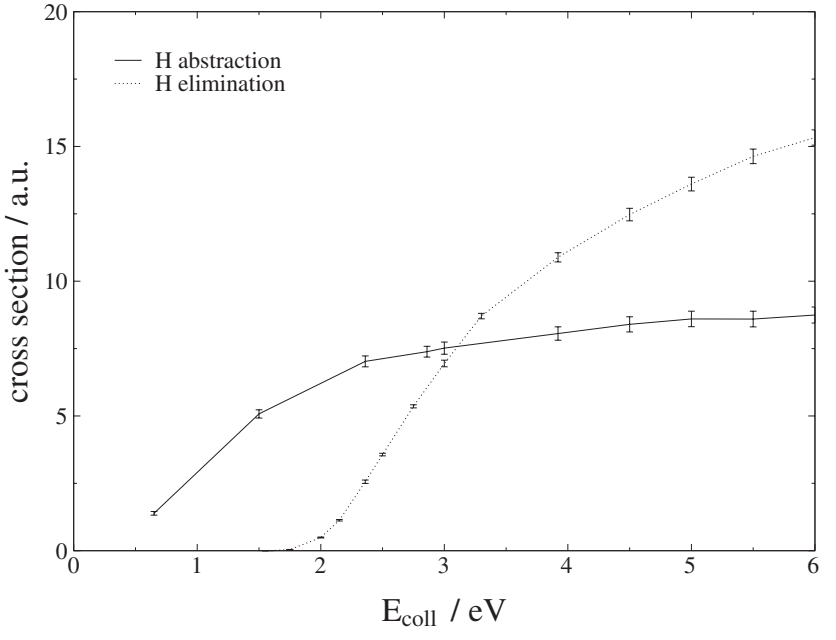

Figure 6. Calculated excitation functions (cross-sections versus collision energy) for the $O(^3P) + CH_4$ reactions.

cross-section is 14% of the total H elimination cross-section. It should be noted that the cross-section ratio between the single and double H elimination channels depends on the time that the trajectories are integrated for. As we shall see below, alkoxy radicals generated in H elimination reactions contain a large amount of internal excitation. This energy is large enough to produce a variety of unimolecular processes. In the case of OCH_3, these include decay to $OCH_2 + H$ and isomerization to CH_2OH. Crossed-beam experiments detect OCH_n species arriving at the detector microseconds after they have been produced. Therefore legitimate comparison with experimental cross-section ratios would require us to integrate the equations of motion for much longer than is feasible at this time. Thus it is more convenient to use primary cross-sections (i.e. the sum of cross-sections for all of the H elimination processes) to make comparison with experiments.

The excitation function for the $O(^3P) + CH_4 \rightarrow OCH_3 + H$ reaction has been measured recently in a crossed-beam experiment carried out at Montana State by the Minton group. The measurements include the threshold region and energies of up to ~1.2 eV above it. These experimental data provide a stringent test for theoretical research aimed at understanding reaction channels that are open only at hyperthermal energies. Comparison with experiments requires explicit calculation of the cross-sections for all of the surfaces that adiabatically correlate from reagents to products. For the $O(^3P) + CH_4 \rightarrow OCH_3 + H$ reaction, there are two surfaces that connect the ground states of the reagents and products. Cross-sections for the lower-energy surface ($1\,^3A$) are presented in figure 6. The corresponding results for the excited surface ($2\,^3A$) are considerably more difficult to obtain even at the MSINDO level as this requires use of configuration interaction (CI) theory. The computational difficulty arises from the general unavailability of analytic gradients for CI calculations, and this is also true in the current implementation of the MSINDO Hamiltonian. Propagation of trajectories is therefore performed using numerical derivatives of the energy, which gives rise to a 20-fold increase in the computation time. Another difficulty is spin contamination in the excited state using unrestricted wavefunctions. This led us to make use of restricted open-shell (ROHF) calculations instead. The suitability of ROHF MSINDO configuration-interaction calculations was examined using more accurate complete active space self-consistent field (CASSCF) *ab initio* calculations.

Figure 7 shows a comparison of the experimental excitation function with the calculated configuration-interaction ROHF MSINDO cross-sections for the $1\,^3A$ and $2\,^3A$ surfaces. There is a ~0.3 eV gap between the thresholds of the experimental and theoretical excitation functions. This was found to be due to the overestimation of the reaction barrier of the ground-state surface by ROHF MSINDO calculations when compared with more accurate *ab initio* data. Aside from this, figure 7 shows that in order for the calculations to match the slope of the experimental excitation function, the contributions of the ground-state ($1\,^3A$) and first-excited ($2\,^3A$) surfaces need to be taken into account explicitly.

Our studies of the hydrogen abstraction channel in $O(^3P) + CH_4$ also enabled us to gain knowledge about triplet–singlet intersystem crossing [226]. The reaction of methane with electronically excited state atomic oxygen ($O(^1D)$) can also generate ground-state $OCH_3 + H$ products. This means that somewhere along the reaction coordinate, the triplet and singlet surfaces must cross. A crossing occurring before the triplet barrier would allow the reaction to occur without surmounting the triplet barrier, so the comparison of excitation functions with

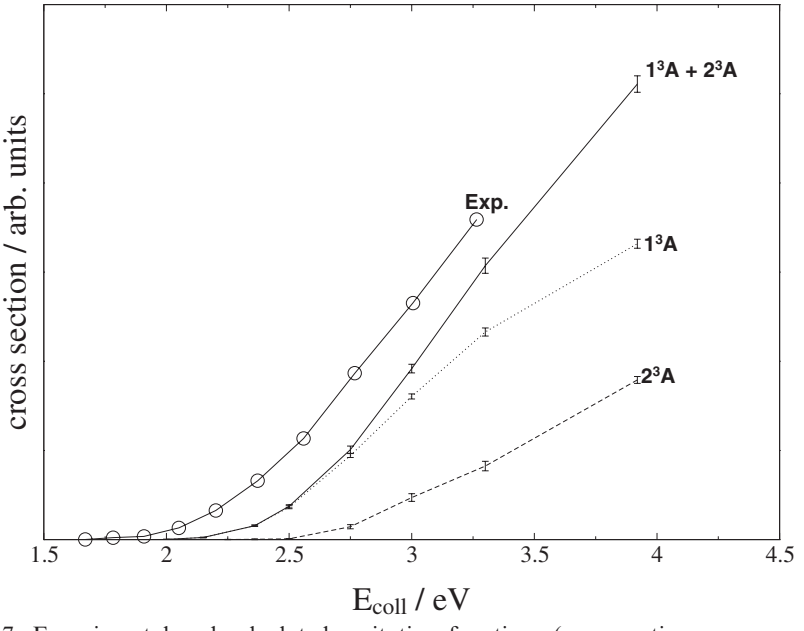

Figure 7. Experimental and calculated excitation functions (cross-sections versus collision energy) for the reaction $O(^3P) + CH_4 \rightarrow OCH_3 + H$.

experiment can be used to determine if intersystem crossing is important. Table 1 indicates that the ground-state barrier for the $O(^3P) + CH_4 \rightarrow OCH_3 + H$ reaction is at ~2 eV. However, before-barrier triplet–singlet crossings were encountered at energies as low as 1.3 eV [217]. Thus, if non-adiabatic transitions are dominant in the region where the surfaces cross, a trajectory departing from the triplet asymptote and hopping to a singlet surface at 1.3 eV would proceed to products without surmounting any additional barrier. This would give rise to a 1.3 eV threshold. Figure 7 indicates that the experimental threshold occurs at ~2 eV, which is the barrier height of the ground-state triplet surface. Therefore, notwithstanding that there are before-barrier triplet-system crossings, the probability for non-adiabatic dynamics at those crossings is negligible, and the experimental excitation function threshold for the $O(^3P) + CH_4 \rightarrow OCH_3 + H$ reaction can be described by triplet-only calculations.

Figure 8 exhibits the excitation functions for the H abstraction, H elimination and C–C breakage reaction channels in collisions of $O(^3P)$ with C_2H_6. H elimination cross-sections comprise $OC_2H_5 + H$ and $OC_2H_4 + H + H$ products, while C–C breakage includes $OCH_3 + CH_3$ and $OCH_2 + CH_3 + H$ products. The multiple-fragment products are always a small fraction of the total cross-section of the corresponding channels in our calculations. The figure shows the difference in the thresholds of the three main reaction channels that is suggested by electronic structure calculations: H abstraction is the lowest-energy process while H elimination and C–C breakage are possible at higher energies. Although the H elimination and C–C breakage barriers are similar, H elimination cross-sections are noticeably larger than the C–C breakage ones (a factor of ~4 in the 4.0–6.0 eV collision energy range). Both the H elimination and C–C cross-sections steadily increase with collision energy in the range explored, but H abstraction is the largest cross-section at all energies. This is a difference between the results for $O(^3P) + CH_4$

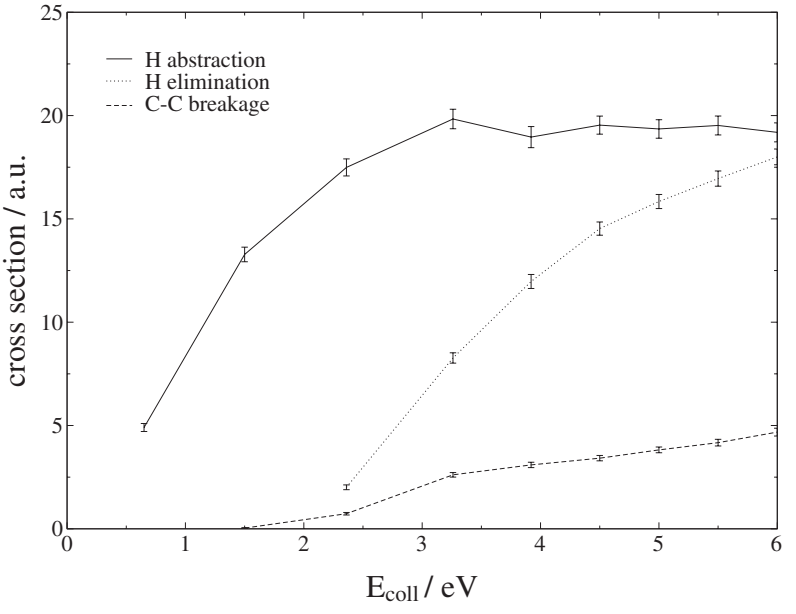

Figure 8. Calculated excitation functions (cross-sections versus collision energy) for the $O(^3P) + C_2H_6$ reactions.

and $O(^3P) + C_2H_6$, where in the former reaction H elimination is the dominant process at the very largest energies calculated. Examination of the saddle-point structures for $O(^3P) + C_2H_6$ indicates that in order for H elimination or C–C breakage to be possible a C–O bond needs to be formed. One may thus interpret that H elimination or C–C breakage are likely to occur when the incoming hyperthermal $O(^3P)$ atoms strikes a carbon atom, adding to the hydrocarbon chain. Concomitantly, H elimination or CH_3 elimination can take place, giving rise to a competition between the H elimination or C–C breakage channels. It is noticeable that at 5 eV (and beyond), the cross-section for processes other than H abstraction (H elimination and C–C breakage) becomes larger than that of H abstraction, in agreement with the $O(^3P) + CH_4$ data.

Figure 9 shows excitation functions for the $O(^3P) + C_3H_8$ reactions. The features of these excitation functions are analogous to those of the reactions with ethane. H abstraction is the lowest-threshold process and dominates at all energies. H elimination and C–C breakage open at ~ 2 eV. The H elimination cross-sections are larger than the C–C breakage ones, and at the largest collision energies explored, the combined H elimination and C–C breakage cross-section is larger than the H abstraction cross-section.

3.2.2. *Energy distributions*

Analysis of energy partitioning in products is an important step towards a complete characterization of the dynamics properties of hyperthermal collisions. Our calculations indicate that the way the available energy is distributed among the product degrees of freedom depends on the reaction channels and on the collision energy. To illustrate these results, average fractions of the available product energy for the most important product channels in reactions associated with $O(^3P) + C_3H_8$ are plotted in figure 10 as a function of collision energy. These fractions depend

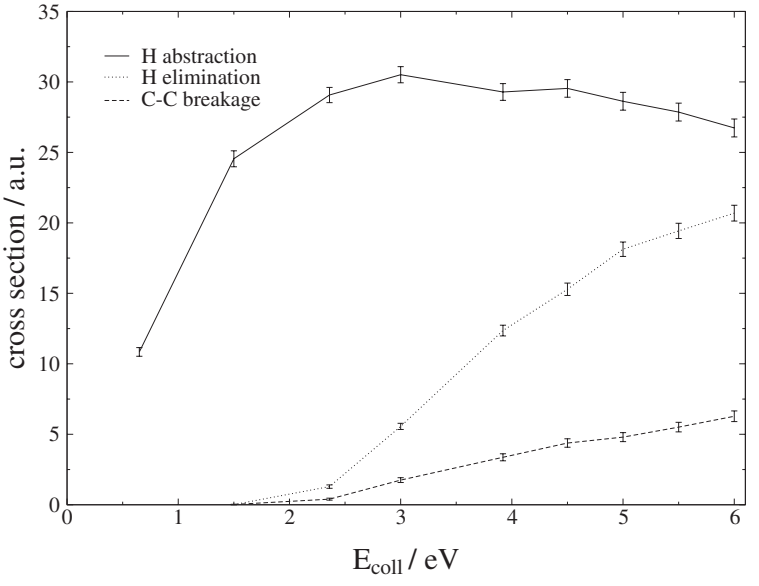

Figure 9. Calculated excitation functions (cross-sections versus collision energy) for the $O(^3P) + C_3H_8$ reactions.

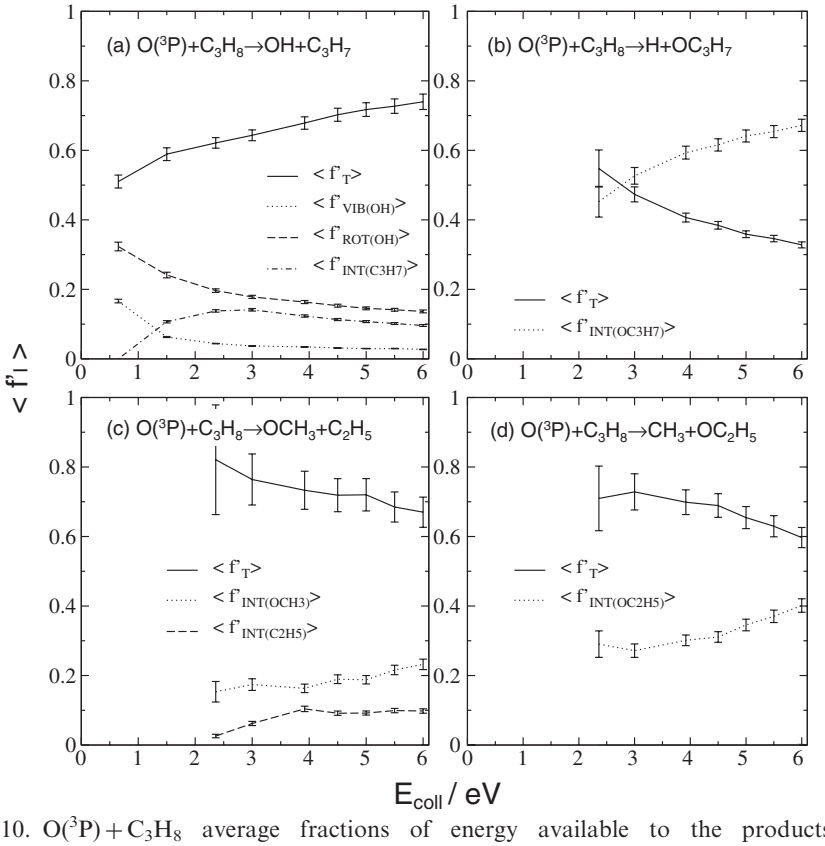

Figure 10. $O(^3P) + C_3H_8$ average fractions of energy available to the products for different reaction pathways: (*a*) $OH + C_3H_7$; (*b*) $H + OC_3H_7$; (*c*) $OCH_3 + C_2H_5$; (*d*) $CH_3 + OC_2H_5$.

slightly on the alkane undergoing reaction with $O(^3P)$, but the trends are similar for reaction with CH_4, C_2H_6 and C_3H_8.

Figure 10(*a*) shows average fractions of energy in products for the H abstraction reaction. Each data point is an average of the fractions for H abstractions in the primary and secondary sites weighted according to the corresponding cross-sections. Energy is preferentially channelled towards product relative translation. This is particularly true at the largest collision energies studied, where only a quarter of the available energy goes to internal degrees of freedom of the product molecules. OH is vibrationally cold at all energies (the population in states other than $v' = 0$ at 5 eV collision energy is < 30%), and so are the propyl radicals. OH rotation seems to receive a significant part of the available energy, but caution should be used when interpreting this result as energy going to rotation has been shown to be over-estimated by the MSINDO Hamiltonian when compared with more accurate dynamics calculations carried out using B3LYP/6-31G* gradients [215].

Average fractions of energy released as relative translation or as propoxy internal energy in the H elimination reactions are plotted in figure 10(*b*). The trends are opposite to those of H abstraction. At hyperthermal energies, there is more energy going to the internal degrees of freedom of the newly formed molecule than to relative translation, and the differences increase with collision energy.

The average fractions of energy in the products of the C–C breakage reaction are shown in figures 10(*c*) ($OCH_3 + C_2H_5$ channel) and 10(d) ($CH_3 + OC_2H_5$ channel). The trends are similar for the two reaction pathways. Energy is preferentially channelled into relative translation. However there is a difference compared to H abstraction such that the fraction of energy in product translation decreases with increasing collision energy. The rest of the energy goes primarily to the newly formed oxy-product, and in the case of the $OC_2H_5 + CH_3$ channel, classical trajectory calculations lead to CH_3 molecules that have less than zero-point energy. (Note that the average fractions of internal energy of CH_3 have been omitted in figure 10(*d*) due to this.)

Some of the trends in figure 10 can be rationalized based on simple triatomic kinematic models [227, 228]. The H abstraction reaction can be described as a light-atom transfer between two heavy moieties, or in other words, a Heavy-Light-Heavy reaction. Study of angular momentum evolution from reagents to products for model H-L-H reactions indicates the presence of an $\mathbf{l} \rightarrow \mathbf{l}'$ correlation, where $\mathbf{l}$ ($\mathbf{l}'$) is the reagent (product) orbital angular momentum. This gives rise to a preferential energy release to product translation. On the other hand, H elimination is better pictured as having Heavy-Heavy-Light kinematics, where the $\mathbf{l} \rightarrow \mathbf{l}'$ correlation does not apply. C–C breakage is not clearly captured by HLH or HHL, and the energy partitioning trends are in-between what can be seen in H abstraction and H elimination, although closer to H abstraction.

4. Reactions of $O(^3P)$ with alkanethiol self-assembled monolayers

Although gas-phase studies provide a wealth of information about the microscopic mechanisms that might be involved in materials degradation in LEO by $O(^3P)$ impact at hyperthermal energies, thorough modelling of polymeric hydrocarbon erosion requires simulation of gas/surface collisions. Several polymeric hydrocarbons, such as polyethylene [193] and polystyrene [189], have been exposed to hyperthermal atomic oxygen in the lab.

We have developed classical trajectory calculations for collisions of $O(^3P)$ with alkanethiolate self-assembled monolayers (SAM's) on Au(111) at hyperthermal energies. The structure of alkanethiol SAM's on gold is well known [229], and its main characteristics can be readily reproduced by theoretical calculations using empirical potentials that contain some *ab initio* information [43, 230]. This contrasts with the difficulties associated with the theoretical description of polymeric materials. Earlier calculations on a similar system but at thermal energies were performed by the Hase group [230].

Our hydrocarbon surface model comprises 37 octanethiolate chains adsorbed in the three-fold hollow sites of an Au(111) surface. A schematic representation of this can be seen in figure 11. As with any reactive system, classical trajectory studies of reactive processes require a suitable interaction potential that allows

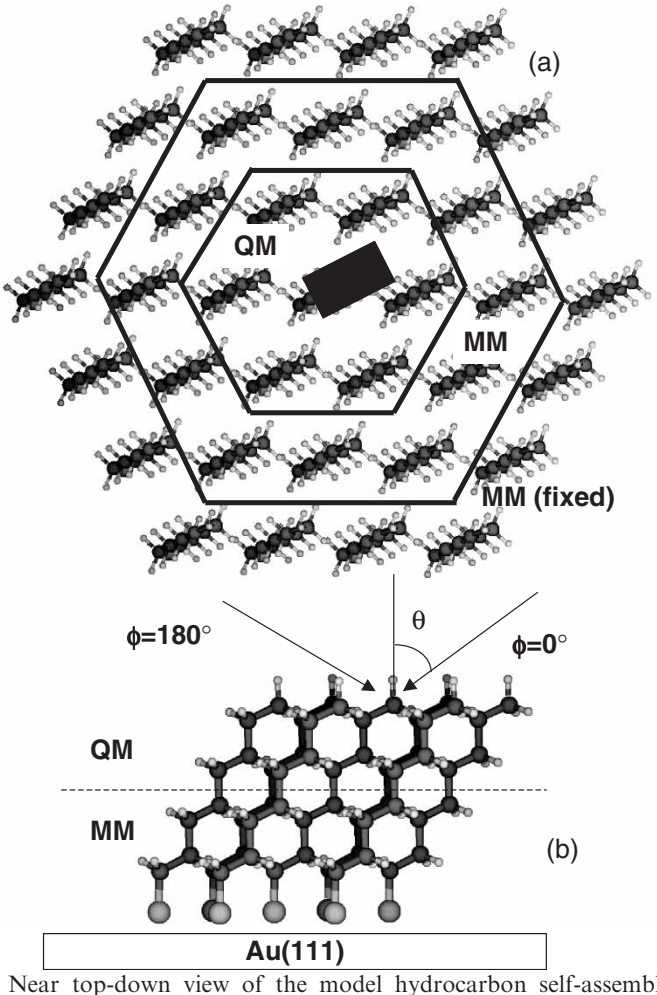

Figure 11. (*a*) Near top-down view of the model hydrocarbon self-assembled monolayer exposed to $O(^3P)$ in the classical trajectory studies described in this work, showing the separation between QM and MM regions. The central shaded area corresponds to the target region. (*b*) Side view of the seven central chains showing the separation between QM/MM regions in those chains. The picture also shows the definition of the incident (θ) and dihedral (ϕ) angle.

for bond breakage and formation. The all-atom direct dynamics approach that we used in the gas-phase studies described above cannot be adopted here due to the poor scaling of computation time of QM techniques with the number of electrons, even at the semi-empirical level. To circumvent this technical difficulty we have used a hybrid quantum mechanics/molecular mechanics (QM/MM) method.

QM/MM methods try to take advantage of the separation of the system into an active and an inactive reaction that can often be imposed in trajectory calculations. The active region is where the most relevant chemical processes (i.e. bond breakage/formation) take place; the inactive region plays a secondary although non-negligible role, and does not experience dramatic changes during the course of the event under study. This philosophy is well-suited for hyperthermal gas/surface collisions. One can imagine that the gas-phase projectile approaching the surface is going to interact strongly with a localized region of the surface in the vicinity of the impact point. If bond breakage or formation is possible, it will occur in this region. On the other hand, there are regions of the surface removed from the impact point that will not be significantly affected by the collision. QM methods are therefore required to properly treat the active region of the surface, while cheaper MM methods can be used for the inactive region.

The QM/MM separation in our $O(^3P) + SAM$ system is depicted in figure 11. We choose a rectangular area around the tip of the central chain of 5×8 a.u. dimensions as the target region for $O(^3P)$ impacts. The central chain and target region are surrounded by six neighbouring hydrocarbon chains. Often, it is seen in the simulations that the $O(^3P)$ or other radical species resulting after interaction with the central chain can be deflected to these neighbouring chains leading to bond breakage and/or formation. It is therefore necessary to treat these six neighbouring chains and the central chain with QM techniques. Generally, $O(^3P)$ or a radical generated in early stages of the trajectory does not have enough translational energy to make it past the six chains surrounding the central chain and strongly interact with outer chains of the surface. Therefore we have limited our QM treatment to the central chain and the six neighbouring chains. The MSINDO Hamiltonian is used to treat this active region of the surface at the QM level.

It should be noted that only the upper half of the chains (butane tips) is treated using QM (see figure 11(*b*)). There are two reasons for this. First, including the anchor sulfur atom and all of the rest of the atoms of the chains in the QM treatment is computationally very cumbersome. Second, recent experimental studies of 5 eV O^+ cations impinging on similar SAM's by Jacobs and coworkers suggest that the reactivity in sites of the SAM below the methyl and two outermost methylene units is minimal [231, 232]. The lower part of the seven central hydrocarbon chains and the rest of the SAM is treated at the MM level using the MM3 force field [233]. The interactions between the sulfur atoms and the gold surface have to be added separately as the MM3 force field does not include parameters for gold atoms.

Classical trajectories are used to simulate collisions of $O(^3P)$ with our model SAM at 5 eV collision energy using the QM/MM model just described. Aside from sampling the target region of the surface defined above, the incident angle (with respect to the surface normal), θ, and the dihedral angle, ϕ, are also sampled. Six batches of 200 trajectories have been run for $\theta = 30$, 45, and 60° for dihedral angles $\phi = 0$ and 180°.

Several phenomena are observed in the calculations. The reactive probabilities follow the trends for the gas-phase cross-sections described above. Inelastic processes dominate, and account for half of the trajectories for most initial conditions. H abstraction to give OH is generally the most probable reaction pathway. This is not surprising given that H abstraction is the lowest-barrier process. However, H elimination is competitive with H abstraction and in some cases is more important, for example with $\theta = 60^\circ$ and $\phi = 0^\circ$. The reason for this is that certain combinations of incident and dihedral angles lead to approach of $O(^3P)$ to the hydrocarbon chains with geometries that overlap with those of minimum-energy reaction paths for H elimination. C–C breakage is a minority channel, much as is found in the gas-phase calculations. The presence of water in the gas/surface calculations is more significant than that in gas-phase studies. H_2O generation is a two-step process whereby an OH radical generated by an H abstraction reaction in the first step produces a second hydrogen abstraction. The second hydrogen atom can be abstracted from the same site where the initial abstraction takes place or from sites in neighbouring chains, and it is this latter process that makes H_2O production so important.

Analysis of product energy distributions indicate the extent to which the two archetypal mechanisms in gas/surface reactions—direct or Eley–Rideal and indirect or Langmuir–Hinshelwood [234]—take place. Direct mechanisms are those in which gas-phase species (usually containing the incoming projectile, but sometimes not) are instantaneously scattered from the surface upon collision, typically with retention of much of the projectile energy, and the product angular distribution has a nearly specular peak. In indirect processes, the gas-phase projectile is trapped on the surface for some time, and energy is accommodated. Large energy transfer occurs and the products are desorbed with energies near to the surface temperature, and in a direction parallel to the surface normal. This process is often termed trapping-desorption.

Our study reveals that large incident angles (i.e. grazing collisions) promote direct events, while initial velocity vectors more parallel to the surface normal enhance trapping-desorption. These are expected trends. Our calculations also reveal that 0° dihedral angle approach produces more trapping-desorption than 180° dihedral angle approach. The reason for this is that 0° dihedral angles provide directions of approach that are parallel to the direction of the alkane chains, and the incoming gas-phase species can fly past the end of the chains of the SAM without losing a large amount of energy (see figure 11(*b*)).

For the product state distributions, the trajectory simulations indicate that OH is mostly generated in its vibrational ground state, irrespective of the microscopic mechanism for reaction, so measurements of this property do not provide a stringent test for differentiating direct from trapping-desorption mechanisms. On the other hand, OH rotation can be more sensitive to reaction mechanism, so if hindered rotation occurs during trapping, rotationally cold OH results, while direct processes give hotter OH. Unfortunately, MSINDO is not a good enough method to quantitatively reproduce measured OH rotational distributions arising from reactions of $O(^3P)$ with saturated alkanes, typically overestimating OH rotational excitation, so its use in simulating O + SAM collisions is unlikely to be accurate. Future higher-quality calculations or experiments using isotopically labelled SAM's will hopefully give more insight into the sensitivity of OH rotation to the reaction mechanism.

Summarizing, simulations of hyperthermal collisions of $O(^3P)$ with model hydrocarbon surfaces confirm the presence of initial reaction pathways other than H abstraction that contribute to degradation. The reaction mechanisms observed have in all cases been anticipated to occur based on gas-phase calculations. However a variety of dynamics phenomena arise from the presence of a soft surface that can trap hyperthermal $O(^3P)$, and this often changes details of the product angular and internal distributions.

5. Concluding remarks

Advances in technology are providing new avenues for research in reaction dynamics. In this paper we have reviewed recent work in gas-phase and gas/surface collisions that occur at hyperthermal energies between neutral species. The research in this field developed by our group has been designed to address the fundamentals of materials degradation in a low Earth orbit environment. Impacts of $O(^3P)$ with spacecraft surfaces at collision energies in the vicinity of 5 eV have been shown to cause oxidation and erosion of the polymeric materials that are used to coat the spacecraft. The development of a reliable and well-characterized hyperthermal atomic oxygen molecular beam in the laboratory has facilitated research at the experimental level, but as we can see from this review, theory also has an important role to play in understanding details of the reaction mechanisms based on quantum mechanical calculations and molecular dynamics simulations.

Quantum mechanics calculations have been performed to characterize the pathways that arise in the reactions of saturated alkanes with $O(^3P)$ at hyperthermal energies. Aside from the well-studied H abstraction pathway that generates OH plus an alkyl radical, two additional and unstudied channels open at energies above ~2 eV. Both processes entail addition of O to the C atoms of the alkane chains. Concomitant elimination of a hydrogen atom produces an alkoxy radical. The addition of oxygen to the hydrocarbon chain can also lead to scission of a C–C bond.

Molecular dynamics simulations of $O(^3P)$ + short-chain alkane reactions have been carried out employing a semi-empirical Hamiltonian that adequately reproduces the fundamental features of the potential energy surface of $O(^3P)$ –alkane systems. Analysis of the excitation functions reveals that at energies close to 5 eV, the combined cross-sections of the reactive channels that open at ~2 eV collision energy (H elimination and C–C breakage) are larger than the cross-sections of the lowest barrier process (H abstraction). This provides new insights toward understanding of alkane processing by hyperthermal $O(^3P)$ in LEO. In addition, classical trajectory simulations of $O(^3P)$ collisions with model condensed-phase hydrocarbons have enhanced our knowledge of the dynamics of the gas/surface collisions.

Combined quantum mechanics and molecular dynamics studies of gas-phase and gas/surface collisions hold excellent promise as modelling tools that will provide detailed information about chemical reactions occurring in extreme environments that have not been explored in detail until now. Improvement in computing capabilities and algorithms together with advances in experimental techniques will provide additional new opportunities for theoretical–experimental interaction, and this activity will doubtless contribute to our progress in developing a molecular level understanding of many important problems.

Acknowledgments

This work has been supported by AFOSR MURI Grant F49620-01-1-0335 and NSF Grant CHE-0131998. The authors wish to thank Timothy Minton (Montana State), Dennis Jacobs (Notre Dame), John Tully (Yale), and Bill Hase (Texas Tech) for fruitful discussions.

References

[1] D. C. Jacobs, Ann. Rev. Phys. Chem. **53**, 379 (2002).
[2] D. C. Jacobs, Chemical Dynamics in Extreme Environments, edited by R. A. Dressler (Singapore: World Scientific), p. 349 (2001).
[3] E. G. Overbosch, and J. Los, Surf. Sci. **108**, 99 (1981).
[4] E. G. Overbosch, and J. Los, Surf. Sci. **108**, 117 (1981).
[5] E. G. Overbosch, B. Rasser, A. D. Tenner, and J. Los, Surf. Sci. **92**, 310 (1980).
[6] A. Danon, and A. Amirav, J. Phys. Chem. **93**, 5549 (1989).
[7] A. Danon, and A. Amirav, Israel J. Chem. **29**, 443 (1989).
[8] Y. Bu, E. F. Greene, and D. K. Stewart, J. Chem. Phys. **92**, 3899 (1990).
[9] A. Danon, A. Vardi, and A. Amirav, Phys. Rev. Lett. **65**, 2038 (1990).
[10] S. Dagan, A. Danon, and A. Amirav, Int. J. Mass Spectrom. Ion Proc. **113**, 157 (1992).
[11] H. Kishi, and T. Fujii, J. Chem. Phys. **108**, 1940 (1998).
[12] H. Kishi, and T. Fujii, Int. J. Mass Spectrom. **194**, 75 (2000).
[13] V. N. Ageev, and S. Y. Davydov, Surf. Sci. **425**, 152 (1999).
[14] B. Bahrim, Teillet-D. Billy, and J. P. Gauyacq, Surf. Sci. **431**, 193 (1999).
[15] C. Bach, and A. Gross, J. Chem. Phys. **114**, 6396 (2001).
[16] G. Katz, Y. Zeiri, and R. Kosloff, Chem. Phys. Lett. **358**, 284 (2002).
[17] J. C. Tully, Ann. Rev. Phys. Chem. **31**, 319 (1980).
[18] M. J. Cardillo, Ann. Rev. Phys. Chem. **32**, 331 (1981).
[19] A. Amirav, M. J. Cardillo, P. L. Trevor, C. Lim, and J. C. Tully, J. Chem. Phys. **87**, 1796 (1987).
[20] C. Lim, J. C. Tully, A. Amirav, P. Trevor, and M. J. Cardillo, J. Chem. Phys. **87**, 1808 (1987).
[21] P. S. Weiss, A. Amirav, P. L. Trevor, and M. J. Cardillo, J. Vac. Sci. Technol. A **6**, 889 (1988).
[22] J. W. P. Hsu, C. C. Bahr, A. V. Felde, D. R. Miller, and M. J. Cardillo, Surf. Sci. **276**, 200 (1992).
[23] M. J. Cardillo, Surf. Sci. **299**, 277 (1994).
[24] K. Burke, J. H. Jensen, and W. Kohn, Surf. Sci. **241**, 211 (1991).
[25] R. J. W. E. Lahaye, S. Stolte, A. W. Kleyn, R. J. Smith, and S. Holloway, Surf. Sci. **307**, 187 (1994).
[26] C. Kim, H. Kang, and S. C. Park, Nucl. Instrum. Meth. Phys. Res. B **95**, 171 (1995).
[27] H. Gades, and H. M. Urbassek, Appl. Phys. A **61**, 39 (1995).
[28] M. E. Saecker, S. T. Govoni, D. V. Kowalski, M. E. King, and G. M. Nathanson, Science **252**, 1421 (1991).
[29] M. E. King, G. M. Nathanson, Hanning-M. A. Lee, and T. K. Minton, Phys. Rev. Lett. **70**, 1026 (1993).
[30] M. E. Saecker, and G. M. Nathanson, J. Chem. Phys. **99**, 7056 (1993).
[31] M. E. King, M. E. Saecker, and G. M. Nathanson, J. Chem. Phys. **101**, 2539 (1994).
[32] G. M. Nathanson, P. Davidovits, D. R. Wornsop, and C. E. Kolb, J. Phys. Chem. **100**, 13007 (1996).
[33] M. E. King, K. M. Fiehrer, G. M. Nathanson, and T. K. Minton, J. Phys. Chem. A **101**, 6556 (1997).
[34] N. Lipkin, R. B. Gerber, N. Moiseyev, and G. M. Nathanson, J. Chem. Phys. **100**, 8408 (1994).
[35] D. Chase, M. Manning, J. A. Morgan, G. M. Nathanson, and R. B. Gerber, J. Chem. Phys. **113**, 9279 (2000).
[36] S. F. Shuler, G. M. Davis, and J. R. Morris, J. Chem. Phys. **116**, 9147 (2002).
[37] B. S. Day, G. M. Davis, and J. R. Morris, Analyt. Chimica Acta. **496**, 249 (2003).

[38] B. S. Day, and J. R. Morris, J. Phys. Chem. B **107**, 7120 (2003).
[39] B. S. Day, S. F. Shuler, A. Ducre, and J. R. Morris, J. Chem. Phys. **119**, 8084 (2003).
[40] M. K. Ferguson, J. R. Lohr, B. S. Day, and J. R. Morris, Phys. Rev. Lett. **92**, 073201 (2004).
[41] K. D. Gibson, N. Isa, and S. J. Sibener, J. Chem. Phys. **119**, 13083 (2003).
[42] N. Isa, K. D. Gibson, T. Yan, W. L. Hase, and S. J. Sibener, J. Chem. Phys. **120**, 2417 (2004).
[43] S. B. M. Bosio, and W. L. Hase, J. Chem. Phys. **107**, 9677 (1997).
[44] T.-Y. Yan, W. L. Hase, and J. R. Barker, Chem. Phys. Lett. **329**, 84 (2000).
[45] T.-Y. Yan, and W. L. Hase, Phys. Chem. Chem. Phys. **2**, 901 (2000).
[46] T.-Y. Yan, and W. L. Hase, J. Phys. Chem. B **106**, 8029 (2002).
[47] T.-Y. Yan, N. Isa, K. D. Gibson, S. J. Sibener, and W. L. Hase, J. Phys. Chem. A **107**, 10600 (2003).
[48] A. P. Graham, and J. P. Toennies, J. Chem. Phys. **118**, 2879 (2003).
[49] S. Mitlin, A. S. Lemak, B. H. Torrie, and K. T. Leung, J. Phys. Chem. B **107**, 9958 (2003).
[50] K. Bolton, M. Svanberg, and J. B. C. Petterson, J. Chem. Phys. **110**, 5380 (1999).
[51] F. H. Geuzebroek, M. E. M. Spruit, and A. W. Kleyn, Surf. Sci. **271**, 207 (1992).
[52] G. C. Weaver, and S. R. Leone, Surf. Sci. **328**, 197 (1995).
[53] A. E. Wiskerke, C. A. Taatjes, A. W. Kleyn, Lahaye, R. J. W. E., S. Stolte, D. K. Bronnikov, and B. E. Hayden, J. Chem. Phys. **102**, 3835 (1995).
[54] C. A. Taatjes, A. E. Wiskerke, and A. W. Kleyn, J. Chem. Phys. **102**, 3848 (1995).
[55] A. E. Wiskerke, and A. W. Kleyn, J. Phys. – Condens. Matter **7**, 5195 (1995).
[56] T. K. Minton, K. P. Giapis, and T. Moore, J. Phys. Chem. A **101**, 6549 (1997).
[57] S. Yagyu, T. Hiraoka, Y. Kino, and S. Yamamoto, Appl. Surf. Sci. **165**, 217 (2000).
[58] M. Korolik, D. W. Arnold, M. J. Johnson, M. M. Suchan, H. Reisler, and C. Wittig, Chem. Phys. Lett. **284**, 164 (1998).
[59] Al-A. Halabi, A. W. Kleyn, and G. J. Kroes, Chem. Phys. Lett. **307**, 505 (1999).
[60] Al-A. Halabi, A. W. Kleyn, and G. J. Kroes, J. Chem. Phys. **115**, 482 (2001).
[61] D. O. N. Gardner, Al-A. Halabi, and G. J. Kroes, Chem. Phys. Lett. **376**, 581 (2003).
[62] Al-A. Halabi, A. W. Kleyn, E. F. Van Dishoeck, M. C. Van Hemert, and G. J. Kroes, J. Phys. Chem. A **107**, 10615 (2003).
[63] Al-A. Halabi, E. F. Van Dishoeck, and G. J. Kroes, J. Chem. Phys. **120**, 3358 (2004).
[64] D. O. N. Gardner, Al-A. Halabi, and G. J. Kroes, J. Phys. Chem. B **108**, 3540 (2004).
[65] Y. Zeiri, and R. R. Lucchese, J. Chem. Phys. **94**, 4055 (1991).
[66] I. Iftimia, and J. R. Manson, Phys. Rev. Lett. **87**, 093201 (2001).
[67] S. T. Ceyer, Ann. Rev. Phys. Chem. **39**, 479 (1988).
[68] G. R. Darling, and S. Holloway, Rep. Prog. Phys. **58**, 1595 (1995).
[69] E. Pijper, G. J. Kroes, R. A. Olsen, and E. J. Baerends, J. Chem. Phys. **117**, 5885 (2002).
[70] S. M. Kingma, M. F. Somers, E. Pijper, G. J. Kroes, R. A. Olsen, and E. J. Baerends, J. Chem. Phys. **118**, 4190 (2003).
[71] R. A. Olsen, G. J. Kroes, and E. J. Baerends, J. Chem. Phys. **111**, 11155 (1999).
[72] A. Cruz, V. Bertin, E. Poulain, J. I. Benitez, and S. Castillo, J. Chem. Phys. **120**, 6222 (2004).
[73] D. J. Oakes, M. R. S. Mccoustra, and M. A. Chesters, Faraday Discuss. Chem. Soc. **96**, 325 (1993).
[74] H. E. Newell, D. J. Oakes, F. J. M. Rutten, M. R. S. Mccoustra, and M. A. Chesters, Faraday Discuss. Chem. Soc. **105**, 193 (1996).
[75] T. Hiraoka, S. Yagyu, T. Kondo, T. Ikeuchi, and S. Yamamoto, Jap. J. Appl. Phys. **39**, 612 (2000).
[76] H. Burghgraef, A. P. J. Jansen, and R. A. Van Santen, Faraday Discuss. Chem. Soc. **96**, 337 (1993).
[77] L. Q. Xia, and J. R. Engstrom, J. Chem. Phys. **101**, 5329 (1994).
[78] R. Milot, A. W. Kleyn, and A. P. J. Jansen, J. Chem. Phys. **115**, 3888 (2001).
[79] M.-N. Carre, and B. Jackson, J. Chem. Phys. **108**, 3722 (1998).
[80] G. Papoian, J. K. Norskov, and R. Hoffmann, J. Am. Chem. Soc. **122**, 4129 (2000).

[81] S. G. Podkolzin, R. Alcala, De J. J. Pablo, and J. A. Dumesic, J. Phys. Chem. B **106**, 9604 (2002).
[82] J. R. Engstrom, L. Q. Xia, M. J. Furjanic, and D. A. Hansen, Appl. Phys. Lett. **63**, 1821 (1993).
[83] T. Ohira, O. Ukai, T. Adachi, Y. Takeuchi, and M. Murata, Phys. Rev. B **52**, 8283 (1995).
[84] J. Tersoff, Phys. Rev. Lett. **68**, 2879 (1988).
[85] D. W. Brenner, Phys. Rev. B **42**, 9458 (1990).
[86] D. W. Brenner, Phys. Rev. B **46**, 1948E (1992).
[87] D. W. Brenner, O. A. Shenderova, J. A. Harrison, S. J. Stuart, B. Ni, and S. B. Sinnott, J. Phys. – Condens. Matter **14**, 783 (2002).
[88] D. R. Alfonso, and S. E. Ulloa, Appl. Phys. Letters **74**, 55 (1999).
[89] D. R. Alfonso, and S. E. Ulloa, Phys. Rev. B **48**, 12235 (1993).
[90] Z. Huang, Z. Y. Pan, W. J. Zhu, Y. X. Wang, and A. J. Du, Surf. Coat. Technol. **141**, 246 (2001).
[91] W. J. Zhu, Z. Y. Pan, Y. K. Ho, and Z. Y. Man, Nucl. Instrum. Meth. Phys. Res. B **153**, 213 (1999).
[92] L. E. Carter, and E. A. Carter, J. Phys. Chem. **100**, 873 (1996).
[93] T. A. Schoolcraft, A. M. Diehl, A. B. Steel, and B. J. Garrison, J. Vac. Sci. Technol. A **13**, 1861 (1995).
[94] A. De Vita, I. Stich, M. J. Gillan, M. C. Payne, and L. J. Clarke, Phys. Rev. Lett. **71**, 1276 (1993).
[95] C. Weissmantel, Thin Films from Free Atoms and Particles, edited by K. J. Klabunde (Orlando, FL: Academic Press), p. 153 (1985).
[96] N. E. Lee, M. Matsuoka, M. R. Sardela, F. Tian, and J. E. Greene, J. Appl. Phys. **80**, 812 (1996).
[97] J. E. Greene, and N. E. Lee, Nucl. Instrum. Meth. Phys. Res. B **121**, 58 (1997).
[98] L. Casalis, M. F. Danisman, B. Nickel, G. Bracco, T. Toccoli, S. Iannotta, and G. Scoles, Phys. Rev. Lett. **90**, 206101 (2003).
[99] Y. Lifshitz, S. R. Kasi, and J. W. Rabalais, Phys. Rev. Lett. **62**, 1290 (1989).
[100] L. F. Qi, and S. B. Sinnott, J. Phys. Chem. B **101**, 6883 (1997).
[101] L. F. Qi, and S. B. Sinnott, Surf. Sci. **398**, 195 (1998).
[102] L. F. Qi, W. L. Young, and S. B. Sinnott, Surf. Sci. **426**, 83 (1999).
[103] T. A. Plaisted, and S. B. Sinnott, J. Vac. Sci. Technol. A **19**, 262 (2001).
[104] X. W. Zhou, and H. N. G. Wadley, Surf. Sci. **431**, 42 (1999).
[105] X. W. Zhou, and H. N. G. Wadley, J. Appl. Phys. **87**, 553 (2000).
[106] G. Chen, I. D. Boyd, S. E. Roadman, and J. R. Engstrom, J. Vac. Sci. Technol. A **16**, 689 (1998).
[107] S. W. Levine, J. R. Engstrom, and P. Clancy, Surf. Sci. **401**, 112 (1998).
[108] J. D'arcy-gall, D. Gall, P. Desjardins, I. Petrov, and J. E. Greene, Phys. Rev. B **62**, 11203 (2000).
[109] Y. G. Yang, X. W. Zhou, R. A. Johnson, and H. N. G. Wadley, Acta Mater. **49**, 3321 (2001).
[110] J. M. Pomeroy, J. Jacobsen, C. C. Hill, B. H. Cooper, and J. P. Sethna, Phys. Rev. B **66**, 235412 (2002).
[111] J. Dalla Torre, G. H. Gilmer, D. L. Windt, R. Kalyanaraman, F. H. Baumann, P. L. O'Sullivan, J. Sapjeta, De La T. D. Rubia, and M. D. Rouhani, J. Appl. Phys. **94**, 263 (2003).
[112] M. A. Hines, Int. Rev. Phys. Chem. **20**, 645 (2001).
[113] D. M. Manos, and D. L. Flamm, Plasma Etching: An Introduction (London: Academic Press, Inc.) (1989).
[114] R. J. Levis, C. J. Waltman, L. M. Cousins, R. G. Copeland, and S. R. Leone, J. Vac. Sci. Technol. A **8**, 3118 (1990).
[115] K. P. Giapis, T. A. Moore, and T. K. Minton, J. Vac. Sci. Technol. A **13**, 959 (1995).
[116] T. Engel, Japanese J. Appl. Phys. **35**, 2403 (1996).
[117] G. S. Hwang, C. M. Anderson, M. J. Gordon, T. A. Moore, T. K. Minton, and K. P. Giapis, Phys. Rev. Lett. **77**, 3049 (1996).

[118] B. J. Garrison, Chem. Soc. Rev. **21**, 155 (1992).
[119] B. J. Garrison, P. B. S. Kodali, and D. Srivastava, Chem. Rev. **96**, 1327 (1996).
[120] B. J. Garrison, A. Delcorte, and K. D. Krantzman, Acc. Chem. Res. **33**, 69 (2000).
[121] A. Galijatovic, A. Darcy, B. Acree, G. Fullbright, R. Mccormac, Green, B., K. D. Krantzman, and T. A. Schoolcraft, J. Phys. Chem. **100**, 9471 (1996).
[122] S. P. Chan, Z. F. Liu, W. M. Lau, and J. S. Tse, Surf. Sci. **432**, 125 (1999).
[123] E. Salonen, K. Nordlund, J. Keikonen, and C. H. Wu, J. Nucl. Mater. **313**, 404 (2003).
[124] T. Lehr, and J. W. Birks, J. Chem. Phys. **70**, 4843 (1979).
[125] N. C. Blais, and D. G. Truhlar, J. Chem. Phys. **74**, 6709 (1981).
[126] N. C. Blais, and D. G. Truhlar, J. Chem. Phys. **78**, 2388 (1983).
[127] J. A. Kaye, and A. Kuppermann, J. Chem. Phys. **84**, 1463 (1986).
[128] J. E. Dove, M. E. Mandy, N. Sathyamurthy, and T. Joseph, Chem. Phys. Lett. **127**, 1 (1986).
[129] M. E. Grice, B. K. Andrews, and W. J. Chesnavich, J. Chem. Phys. **87**, 959 (1987).
[130] N. C. Blais, D. G. Truhlar, and C. A. Mead, J. Chem. Phys. **89**, 6204 (1988).
[131] H. R. Mayne, Int. Rev. Phys. Chem. **10**, 107 (1991).
[132] J. B. Song, Chem. Phys. **285**, 255 (2002).
[133] K. Sakimoto, Chem. Phys. **236**, 123 (1998).
[134] K. Sakimoto, J. Chem. Phys. **110**, 11233 (1999).
[135] K. Sakimoto, J. Chem. Phys. **112**, 5044 (2000).
[136] K. Nobusada, K. Sakimoto, and K. Onda, Chem. Phys. Lett. **216**, 613 (1993).
[137] K. Sakimoto, Chem. Phys. Lett. **228**, 323 (1994).
[138] K. Nobusada, K. Sakimoto, and K. Onda, Chem. Phys. Lett. **233**, 399 (1995).
[139] K. Sakai, Chem. Phys. **220**, 115 (1997).
[140] K. Nobusada, and K. Sakimoto, Chem. Phys. Lett. **288**, 311 (1998).
[141] W. Jakubetz, Connor, J. N. L, and P. J. Kuntz, Phys. Chem. Chem. Phys. **1**, 1213 (1999).
[142] T. Takayanagi, and A. Wada, J. Chem. Phys. **115**, 6385 (2001).
[143] T. Takayanagi, and A. Wada, Chem. Phys. **277**, 313 (2002).
[144] P. G. Martin, W. J. Keogh, and M. E. Mandy, AstroPhys. J. **499**, 793 (1998).
[145] A. Ceballos, E. Garcia, A. Rodriguez, and A. Lagana, Chem. Phys. Lett. **305**, 276 (1999).
[146] A. Ceballos, E. Garcia, and A. Lagana, J. Phys. Chem. Ref. Data **31**, 371 (2002).
[147] M. I. Hernandez, and D. C. Clary, J. Chem. Phys. **104**, 8413 (1996).
[148] Di D. Domenico, M. I. Hernandez, and J. Campos-Martinez, Chem. Phys. Lett. **342**, 177 (2001).
[149] D. Di Domenico, M. I. Hernandez, and J. Campos-Martinez, J. Chem. Phys. **115**, 7897 (2001).
[150] B. Y. Pan, and J. M. Bowman, J. Chem. Phys. **103**, 9661 (1995).
[151] G. S. Whittier, and J. C. Light, J. Chem. Phys. **110**, 4280 (1999).
[152] R. Kaiser, and A. Mebel, Int. Rev. Phys. Chem. **21**, 307 (2002).
[153] De Sainte P. Claire, G. H. Peslherbe, and W. L. Hase, J. Phys. Chem. **99**, 8147 (1995).
[154] De Sainte P. Claire, and W. L. Hase, J. Phys. Chem. **100**, 8190 (1996).
[155] L. Poisson, P. De Pujo, V. Brenner, A. L. Derepas, J. P. Dognon, and J. M. Mestdagh, J. Phys. Chem. A **106**, 1714 (2002).
[156] R. G. Cooks, T. Ast, T. Pradeep, and V. Wysocki, Acc. Chem. Res. **27**, 316 (1994).
[157] A. W. Kleyn, J. Phys. – Condens. Matter **4**, 8375 (1992).
[158] E. Kolodney, D. Baugh, P. S. Powers, H. Reisler, and C. Wittig, J. Chem. Phys. **90**, 3883 (1989).
[159] E. Kolodney, P. S. Powers, L. Hodgson, H. Reisler, and C. Wittig, J. Chem. Phys. **94**, 2330 (1991).
[160] P. S. Powers, E. Kolodney, L. Hodgson, G. Ziegler, H. Reisler, and Wittig, C., J. Phys. Chem. **95**, 8387 (1991).
[161] H. Ferkel, J. T. Singleton, H. Reisler, and C. Witting, Chem. Phys. Lett. **221**, 447 (1994).
[162] D. W. Arnold, M. Korolik, C. Wittig, and H. Reisler, Chem. Phys. Lett. **282**, 313 (1998).

[163] E. Por, and M. Asscher, J. Chem. Phys. **90**, 3405 (1989).
[164] C. Akerlund, I. Zoric, B. Kasemo, A. Cupolillo, De F. B. Mongeot, and M. Rocca, Chem. Phys. Lett. **270**, 157 (1997).
[165] S. P. Lohokare, E. L. Crane, L. H. Dubois, and R. G. Nuzzo, J. Chem. Phys. **108**, 8640 (1998).
[166] D. Kulnigov, M. Persson, and C. T. Rettner, J. Chem. Phys. **106**, 3370 (1997).
[167] J. D. Beckerle, A. D. Johnson, and S. T. Ceyer, Phys. Rev. Lett. **62**, 685 (1989).
[168] K. Karahashi, J. Matsuo, and H. Horiuchi, Surf. Sci. **358**, 800 (1996).
[169] L. Vattuone, P. Gambardella, F. Cemic, U. Valbusa, and M. Rocca, Chem. Phys. Lett. **278**, 245 (1997).
[170] L. Vattuone, P. Gambardella, U. Burghaus, F. Cemic, A. Cupolillo, U. Valbusa, and M. Rocca, J. Chem. Phys. **109**, 2490 (1998).
[171] U. Valbusa, F. B. De Mongeot, M. Rocca, and L. Vattuone, Vacuum **50**, 445 (1998).
[172] T. Takaoka, M. Terahara, and I. Kusunoki, Surf. Sci. **454**, 218 (2000).
[173] J. Libuda, and G. Scoles, J. Phys. Chem. B **103**, 9933 (1999).
[174] J. Libuda, and G. Scoles, J. Chem. Phys. **112**, 1522 (2000).
[175] L. Romm, Y. Zeiri, and M. Asscher, J. Chem. Phys. **108**, 8605 (1998).
[176] Y. Zeiri, and R. R. Lucchese, Surf. Sci. **264**, 197 (1992).
[177] M. Asscher, L. Romm, and Y. Zeiri, Coll. Surf. A **208**, 187 (2002).
[178] L. Sun, De Sainte P. Claire, O. Meroueh, and W. L. Hase, J. Chem. Phys. **114**, 535 (2001).
[179] M. Asscher, and Y. Zeiri, J. Phys. Chem. B **107**, 6903 (2003).
[180] K. J. Maynard, A. D. Johnson, S. P. Daley, and S. T. Ceyer, Faraday Discuss. Chem. Soc. **91**, 437 (1991).
[181] J. T. Kindt, and J. C. Tully, J. Chem. Phys. **111**, 11060 (1999).
[182] Y. Zeiri, J. Chem. Phys. **113**, 3868 (2000).
[183] L. J. Leger, and J. T. Visentine, J. Spacecraft Rockets **23**, 505 (1986).
[184] L. E. Murr, and W. H. Kinard, Am. Sci. **81**, 152 (1993).
[185] A. Jursa, US Standard Atmosphere (Washington: US Government Printing Office) (1976).
[186] Z. A. Iskanderova, J. I. Kleiman, Y. Gudimenko, and R. C. Tennyson, J. Spacecraft Rockets **32**, 878 (1995).
[187] B. Cazaubon, A. Paillous, J. Siffre, and R. Thomas, J. Spacecraft Rockets **35**, 797 (1998).
[188] E. Grossman, Y. Lifshitz, J. T. Wolan, C. K. Mount, and G. B. Hoflund, J. Spacecraft Rockets **36**, 75 (1999).
[189] T. K. Minton, J. Zhang, D. J. Garton, and J. W. Seale, High Perform. Polym. **12**, 27 (2000).
[190] H. Kinoshita, M. Tagawa, K. Yokota, and N. Ohmae, High Perform. Polym. **13**, 225 (2001).
[191] K. Yokota, M. Tagawa, and N. Ohmae, J. Spacecraft Rockets **40**, 143 (2003).
[192] H. Kinoshita, M. Umeno, M. Tagawa, and N. Ohmae, Surf. Sci. **440**, 49 (1999).
[193] J. Zhang, and T. K. Minton, High Perform. Polym. **13**, S467 (2001).
[194] K. T. Nicholson, T. K. Minton, and S. J. Sibener, Prog. Org. Coat. **47**, 443 (2003).
[195] K. L. Kelly, H. Decornez, J. C. Tully, K. T. Nicholson, S. J. Sibener, and T. K. Minton, to be submitted (2004).
[196] T. K. Minton, and D. J. Garton, Chemical Dynamics in Extreme Environments, edited by R. A. Dressler (Singapore: World Scientific), p. 420 (2001).
[197] M. Tagawa, T. Ema, H. Kinoshita, N. Ohmae, M. Umeno, and T. K. Minton, Jap. J. Appl. Phys. **37**, L1455 (1998).
[198] M. Tagawa, K. Yokota, N. Ohmae, H. Kinoshita, and M. Umeno, Jap. J. Appl. Phys. **40**, 6152 (2001).
[199] M. Randjelovic, and J. C. Yang, Mater. High Temp. **20**, 281 (2003).
[200] A. Houdayer, G. Cerny, J. E. Klembergsapieha, G. Czeremuszkin, and M. R. Wertheimer, Nucl. Instrum. Meth. Phys. Res. B **131**, 335 (1997).
[201] R. I. Gonzalez, S. H. Phillips, and G. B. Hoflund, J. Spacecraft Rockets **37**, 463 (2000).

[202] G. B. Hoflund, R. I. Gonzalez, and S. H. Phillips, J. Adhes. Sci. Technol. **15**, 1199 (2001).
[203] E. Wisotzki, A. G. Balogh, H. Hahn, J. T. Wolan, and G. B. Hoflund, J. Vac. Sci. Technol. A **17**, 14 (1999).
[204] J. J. Osborne, G. T. Roberts, A. R. Chambers, and S. B. Gabriel, Sens. Actuat. B **63**, 55 (2000).
[205] J. F. Weaver, T. J. Campbell, G. B. Hoflund, and G. N. Salaita, J. Electron Spectros. Rel. Phenom. **106**, 81 (2000).
[206] Y. Li, and J. C. Yang, Mater. High Temp. **20**, 601 (2003).
[207] R. H. Krech, M. J. Gauthier, and G. E. Caledonia, J. Spacecraft Rockets **30**, 509 (1993).
[208] J. Zhang, D. J. Garton, and T. K. Minton, J. Chem. Phys. **117**, 6239 (2002).
[209] D. M. Sonnenfroh, and G. E. Caledonia, J. GeoPhys. Res. **98**, 21605 (1993).
[210] Lee, C.-H, and L. W. Chen, J. Spacecraft Rockets **37**, 252 (2000).
[211] D. J. Mann, and M. D. Halls, J. Chem. Phys. **116**, 9014 (2002).
[212] A. Gindulyte, L. Massa, B. A. Banks, and S. K. Rutledge, 2000, J. Phys. Chem. A **104**, 9976.
[213] A. Gindulyte, L. Massa, B. A. Banks, and S. K. R. Miller, J. Phys. Chem. A **106**, 5463 (2002).
[214] D. J. Garton, T. K. Minton, D. Troya, R. Pascual, and G. C. Schatz, J. Phys. Chem. A **107**, 4583 (2003).
[215] D. Troya, R. Z. Pascual, and G. C. Schatz, J. Phys. Chem. A **107**, 10497 (2003).
[216] D. Troya, R. Z. Pascual, D. J. Garton, T. K. Minton, and G. C. Schatz, J. Phys. Chem. A **107**, 7161 (2003).
[217] D. Troya, G. C. Schatz, D. J. Garton, A. L. Brunsvold, and T. K. Minton, J. Chem. Phys. **120**, 731 (2004).
[218] D. J. Garton, T. K. Minton, B. Maiti, D. Troya, and G. C. Schatz, J. Chem. Phys. **118**, 1585 (2003).
[219] P. Andresen, and A. C. Luntz, J. Chem. Phys. **72**, 5842 (1980).
[220] F. Ausfelder, and K. G. Mckendrick, Prog. React. Kinet. Mechan. **25**, 299 (2000).
[221] D. L. Baulch, C. J. Cobos, R. A. Cox, C. Esser, P. Frank, Just, T., Kerr, J. A., M. J. Pilling, J. Troe, R. W. Walker, and J. Warnatz, J. Phys. Chem. Ref. Data **21**, 411 (1992).
[222] N. Cohen, and K. R. Westberg, J. Phys. Chem. Ref. Data **20**, 1211 (1991).
[223] T. Yan, W. L. Hase, and C. Doubleday, J. Chem. Phys. **120**, 9253 (2004).
[224] B. Ahlswede, and K. Jug, J. Comput. Chem. **20**, 563 (1999).
[225] G. C. Schatz, J. Phys. Chem. **100**, 12839 (1996).
[226] B. Maiti, and G. C. Schatz, J. Chem. Phys. **119**, 12360 (2003).
[227] R. D. Levine, and R. B. Bernstein, Molecular Reaction Dynamics and Chemical Reactivity (Oxford: Oxford University Press) (1987).
[228] I. Schechter, R. D. Levine, and R. G. Gordon, J. Phys. Chem. **95**, 8201 (1991).
[229] Camilone III, N., Chidsey, C. E. D., P. Eisenberger, P. Fenter, Li, J., Liang, K. S., Liu, G.-Y, and G. Scoles, J. Chem. Phys. **99**, 744 (1993).
[230] G. Li, S. B. M. Bosio, and W. L. Hase, J. Mol. Struct. **556**, 43 (2000).
[231] X. Qin, T. Tzvetkov, and D. C. Jacobs, Nucl. Instrum. Meth. Phys. Res. B **203**, 130 (2003).
[232] X. Qin, T. Tzvetkov, and D. C. Jacobs, Private communication (2004).
[233] N. L. Allinger, Y. H. Yuh, and J.-H. Lii, J. Am. Chem. Soc. **111**, 8551 (1989).
[234] C. T. Rettner, and D. J. Auerbach, Science **263**, 365 (1994).